Defense Threat Reduction Agency
8725 John J. Kingman Road, MS
6201 Fort Belvoir, VA 22060-6201

DTRA-TR-20-02

TECHNICAL REPORT

Radiation Survivability of MEMS Microelectronic Circuits with Carbon Nanotube Field Emitters

January 2020

HDTRA1-15-1-0071

Prepared by: Jason J Amsden, Duke University
Durham, NC 27708

REPORT DOCUMENTATION PAGE

Form Approved
OMB No. 0704-0188

1. REPORT DATE *(DD-MM-YYYY)*	2. REPORT TYPE	3. DATES COVERED *(From - To)*
11/27/2019	Final Report	9/1/2015 - 8/31/2019

4. TITLE AND SUBTITLE
Radiation survivability of MEMS microelectronic circuits with carbon nanotube field emitters

5a. CONTRACT NUMBER

5b. GRANT NUMBER
HDTRA1-15-1-0071

5c. PROGRAM ELEMENT NUMBER

6. AUTHOR(S)
Amsden, Jason J.; Gilchrist, Kristin H., Glass, Jeffrey T., Parker, Charles. B. Windheim, Tasso von

5d. PROJECT NUMBER

5e. TASK NUMBER

5f. WORK UNIT NUMBER

7. PERFORMING ORGANIZATION NAME(S) AND ADDRESS(ES)
DUKE UNIVERSITY 2200 W MAIN ST STE 710 DURHAM NC 27708-4677,
RTI International 3040 East Cornwallis Road, P.O. Box 12194 Research Triangle Park, NC, United States 27709-2194

8. PERFORMING ORGANIZATION REPORT NUMBER

9. SPONSORING/MONITORING AGENCY NAME(S) AND ADDRESS(ES)
Defense Threat Reduction Agency
8725 John J. Kingman Road
Fort Belvoir, VA 22060-6201

10. SPONSOR/MONITOR'S ACRONYM(S)
DTRA

11. SPONSOR/MONITOR'S REPORT NUMBER(S)

12. DISTRIBUTION/AVAILABILITY STATEMENT

DISTRIBUTION STATEMENT A: Approved for public release, distribution is unlimited

13. SUPPLEMENTARY NOTES

14. ABSTRACT

The objective of this program was to determine the effects of radiation on MEMS vacuum microelectronic devices with integrated carbon nanotube field emitters. We do observe some small effects of radiation on the field emission properties of CNTs and integrated MEMS vacuum microelectronic devices. However, the residual gas in the vacuum chamber adsorbing and desorbing from the surface of the CNTs has a much larger effect on field emission and device performance than the radiation

15. SUBJECT TERMS
MEMS, CNT, field emission, radiation effects

16. SECURITY CLASSIFICATION OF:			17. LIMITATION OF ABSTRACT	18. NUMBER OF PAGES	19a. NAME OF RESPONSIBLE PERSON
a. REPORT	b. ABSTRACT	c. THIS PAGE			Jacob A Calkins
					19b. TELEPHONE NUMBER *(Include area code)*
U	U	U	UU	45	571-616-5946

Radiation survivability of MEMS microelectronic circuits with carbon nanotube field emitters

Final Report

December 2019

Grant No. HDTRA1-15-1-0071

DTRA Program Manager **Dr. Jacob Calkins (jacob.a.calkins.civ@mail.mil**	
Team	
Dr. Jason J. Amsden (PI) **Dr. Jeffrey T. Glass (Co-PI)** **Duke University**	**Dr. Kristin H. Gilchrist** **RTI International**

Technical Point of Contact
Dr. Jason J. Amsden (jason.amsden@duke.edu); 9193481574
Duke University Department of Electrical and Computer Engineering1 00 Science Drive, 130 Hudson Hall, Box 90291, Durham, NC 27708

Administrative Point of Contact
Susan Lasley (susan.lasley@duke.edu); 9196818684
Office of Research Support, Duke University, Box 104010, Durham NC 27708

1 Executive summary

Solid-state technology dominates the consumer electronics market because of the low cost associated with large-scale integration. However, there are numerous applications in which solid-state devices are unreliable or do not provide adequate performance, particularly in applications with systems operating in extreme environments such as environments with elevated radiation levels. In these applications, vacuum microelectronic devices present an attractive alternative. Despite the performance advantages, the use of vacuum electronics has been limited because there is no versatile and reliable microscale platform that enables integration of large numbers of vacuum circuit elements on a single substrate. To address this need, RTI International in collaboration with Duke University have been developing a Microelectromechanical systems (MEMS) platform with carbon nanotube (CNT) field emitters that enables integration of high-performance microelectronic vacuum components into functional circuits on a single silicon substrate. While these devices avoid the radiation-induced charge carrier problems in solid-state devices, other effects of radiation on this MEMS platform have not been studied. The objective of this program was to determine the effects of radiation on this device platform to validate its use for applications requiring radiation hardness.

The project involved work on seven different tasks. These tasks are listed below along with a brief summary of the major activities and outcomes. Detailed descriptions of the experiments performed and the results obtained are divided into four subsequent sections including: Section 2 – Determination of radiation effects on the MEMS platform; Section 3 - Comparing field emission performance of different carbon nanostructures; Section 4 - Effects of gamma and proton radiation on aligned CNT field emitters; and Section 5 - Design, fabrication, and characterization of a polysilicon MEMS NOR gate vacuum microelectronic device with integrated CNT field emitters. As described in the sections below, while we do observe some small effects of radiation on the field emission properties of CNTs and integrated MEMS vacuum microelectronic devices, the residual gas in the vacuum chamber adsorbing and desorbing from the surface of the CNTs has a much larger effect on field emission and device performance than the radiation. Section 6 provides suggestions for future work.

Task 1: Determine the effects of radiation on the field emission properties of carbon nanostructures.

- Activities related to this tasks included comparing the field emission performance of different carbon nanostructures including aligned CNTs, graphenated CNTs, and aligned-graphenated CNTs (see section 3), and investigating the effects of gamma and proton radiation on the field emission properties of aligned CNTs before and after radiation exposure (see section 4). Results indicated that aligned CNTs have better performance than either graphenated CNTs or aligned-graphenated CNTs. Therefore, we used aligned CNTs for studying the radiation effects. When investigating the radiation effects on field emission, we found that gamma and proton radiation both decrease the defect density in CNTs, and this contributes to increased turn-on field in the samples. Other than the increase in turn-on field, we did not observe any other effects of radiation. We suspect that any changes in field emission due to radiation, other than turn-on voltage, were

masked by the effects of residual gas adsorbing and desorbing from the surface of the CNTs which cause large fluctuations in field emission current.

Task 2: Design and build test chamber for *in situ* measurements of radiation effects.

- Activities related to this task included some work on developing a miniature vacuum chamber by bonding an aluminum chamber to a pin grid array. However, due to many requests from other users of their facility, NASA JPL constructed a vacuum chamber. Therefore, we discontinued work on our miniature vacuum chamber, and we used the NASA JPL chamber for *in situ* testing.

Task 3: Design and fabricate polysilicon MEMS for mechanical and electrical testing without field emission.

- Activities related to this task included designing 2 different resistor structures using the MEMS platform. See section 2 for additional details.

Task 4: Characterize radiation effects of polysilicon MEMS devices without field emission.

- Activities related to this task included exposing the resistor structures designed and fabricated in task 3 to proton and gamma radiation. We observed a very small dose dependent reduction in resistance by less than 0.5% for radiation exposures up to 3 Mrad(Si). See section 2 for additional details.

Task 5: Design, model, and fabricate two representative polysilicon MEMS devices with integrated field emitters.

- Activities for these tasks included design and fabrication of a simple two-panel MEMS device consisting of a cathode and anode as well as a much more complex NOR gate comprised of two MEMS tetrodes with CNT field emitters. Section 5 presents details on the design, modeling, fabrication and performance of the MEMS NOR gate.

Task 6: Evaluate the field emission properties of the carbon nanostructures while they are under irradiation.

- Given the limited effects of radiation on the MEMS platform, we combined task 6 with task 7

Task 7: Characterize the effects of radiation on *in situ* operation of polysilicon MEMS with integrated field emission cathodes.

- Activities related to this task included packaging several of the simple two-panel MEMS devices fabricated in task 5 for *in situ* exposure to gamma radiation. We evaluated the field emission performance of these devices by measuring the voltage variation required to maintain a constant emission current with and without exposure to radiation. For low currents the rate of voltage variation is smaller during exposure to radiation due to a small background current caused by ionization of residual gas in the vacuum chamber by the gamma radiation. For higher currents, the voltage variation required to maintain a

constant emission current is similar with and without radiation exposure. See section 4 and subsections 4.2.5 and 4.3.4 for additional details. *in situ* measurements using proton radiation were not possible. The high energy proton radiation from the UC Davis facility induced significant radiation in our sample support structures, therefore, we were not able to do *in situ* measurements due to the possibility of inducing radioactivity in the vacuum chamber.

This program has supported researchers at Duke University, RTI International, and NASA JPL. The table below lists the personnel, title, and organization.

Name	Personnel Type	Organization
Jason J. Amsden	PI	Duke University
Kristin Gilchrist	Co-PI	RTI International
Jeffrey T. Glass	Co-PI	Duke University
Tasso von Windheim	Graduate Student	Duke University
Erich Radauscher	Graduate Student	Duke University
James Thostenson	Graduate Student	Duke University
Yihao Zhou	Graduate Student	Duke University
Tanouir Aloui	Graduate Student	Duke University
Stephen Ubnoske	Research Associate/Scientist	Duke University
Nick Baldasaro	Research Associate/Scientist	RTI International
Jim Carlson	Research Associate/Scientist	RTI International
Leif Scheick	Research Associate/Scientist	NASA JPL
Charles B. Parker	Research Associate/Scientist	Duke University
Brian R. Stoner	Research Associate/Scientist	RTI International/Duke University
Bernard Rax	Research Associate/Scientist	NASA JPL
David Stokes	Research Associate/Scientist	RTI International
Erik Vik	Research Associate/Scientist	RTI International

2 Determination of radiation effects on the MEMS platform

2.1 Introduction

Polysilicon surface micromachining is a well-established technique for fabricating a wide range of geometrically complex MEMS structures including free-standing structures extending outward from the substrate [1]. Fabricating devices from freestanding polysilicon panels provides many benefits for an integrated vacuum circuit platform. This fabrication technology is highly versatile because the number of process steps does not increase with increasing device complexity or increasing numbers of devices. All device structures are formed on a single substrate, so there is no need to align external components or integrate multiple substrates. Freestanding panel structures also offer the advantage of low capacitance to ground and therefore high-speed capability. Finally, supporting elements such as resistors and inductors can be easily incorporated in this technology and can also be made freestanding. We have demonstrated a wide variety of vacuum electronic devices using the freestanding panel approach fabricated with the Polysilicon Multi-User MEMS Process (PolyMUMPs) [2-5]. Figure 1 (a) shows two integrated triode structures with a shared cathode panel [6], Figure 1 (b) and (c) show a scanning electron microscope (SEM) image of an ion source for a miniature mass spectrometer [4].

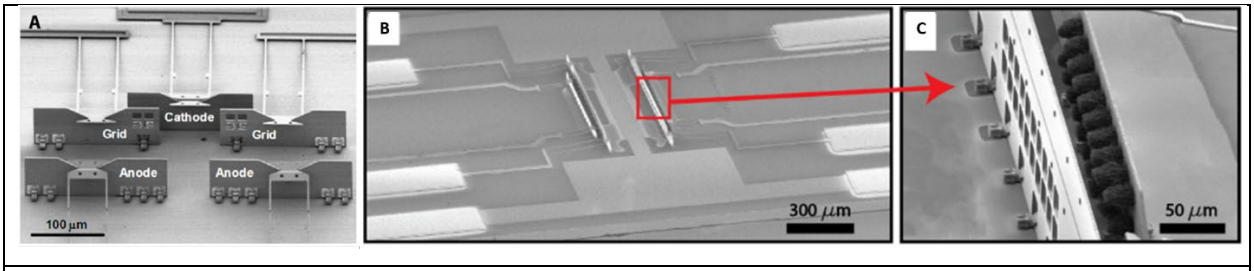

Figure 1: SEM image of two integrated triodes fabricated from vertical polysilicon panels panel (a) [6]. SEM image of a MEMS ion source with a CNT field emission cathode panel (b and c) [4].

The effects of radiation on polysilicon MEMS devices have been studied in the past [7-9]. Radiation studies on MEMS indicate that the mechanical properties of the polysilicon in the MEMS platform will likely remain unchanged under radiation. However, the carrier mobility can decrease leading to increased resistivity [9]. Here, we fabricated several resistor structures in the MEMS platform and quantified the resistivity increase for gamma radiation. We observed a very small dose-dependent reduction in resistance by less than 0.5% for radiation exposures up to 3 Mrad(Si).

2.2 Experimental details

To investigate the dose-dependent electrical properties of the MEMS platform, we fabricated both attached and released resistor structures using the polyMUMPs platform and measured the resistance of the structures using a 4-point probe apparatus.

2.2.1 MEMS fabrication

Resistors of varying geometry were fabricated via Polysilicon Multi-User MEMS Processes (PolyMUMPs). PolyMUMPs is a commercial process designed for cost-effective, general-purpose micromachining of polysilicon structures. The process includes two structural layers of polysilicon, Poly1 and Poly2. Poly1 is a 2 μm thick film with a typical resistivity of 10 ohm/sq and Poly2 is a 1.5 μm thick film with a typical resistivity of 20 ohm/sq [2]. To capture a wide range of resistance, we fabricated 1 mm long resistors in both layers in widths of 25 μm and 50 μm. The PolyMUMPs process enables fabrication of resistors which are attached to an insulating substrate as well as released structures, where the underlying oxide layer is removed to create freestanding beams with an air gap underneath, as shown in Figure 2 (a). We fabricated both types of resistors as shown in the microscope image of Figure 2 (b).

(a)

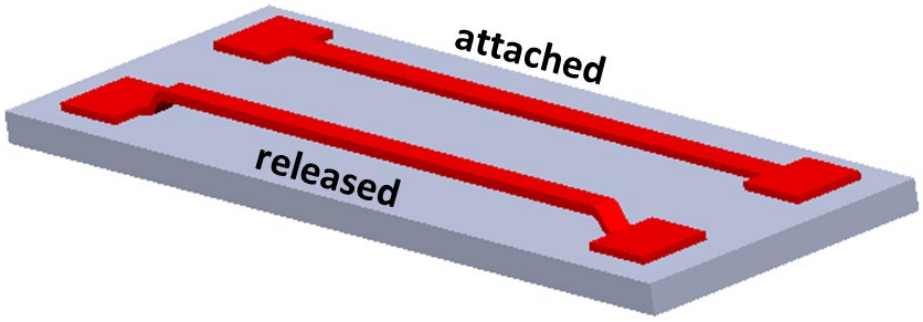

(b)

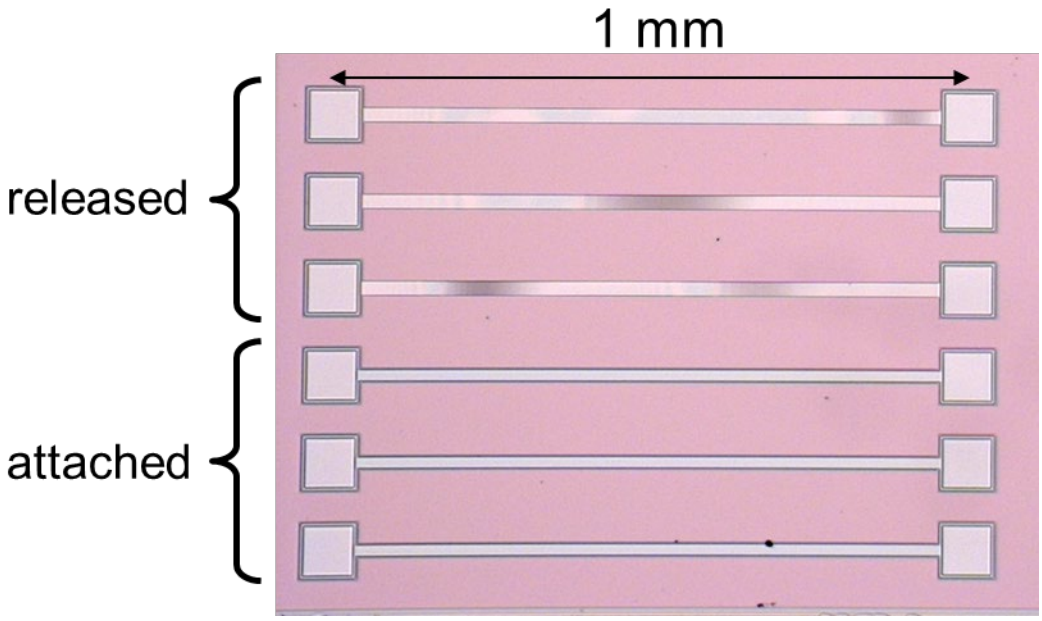

Figure 2: Diagram of the resistors used to investigate potential radiation effects on the polysilicon MEMS platform (a). Microscope image with scale bar of the resistors (b).

2.2.2 Resistance measurements

To determine the resistance of the devices, we performed a four-point probe measurement with a Keithley 2410 source meter and LabView software. See Figure 3 for a diagram of the four-point probe measurement set up. Resistance was computed from a linear fit to IV data taken from 0-5 V.

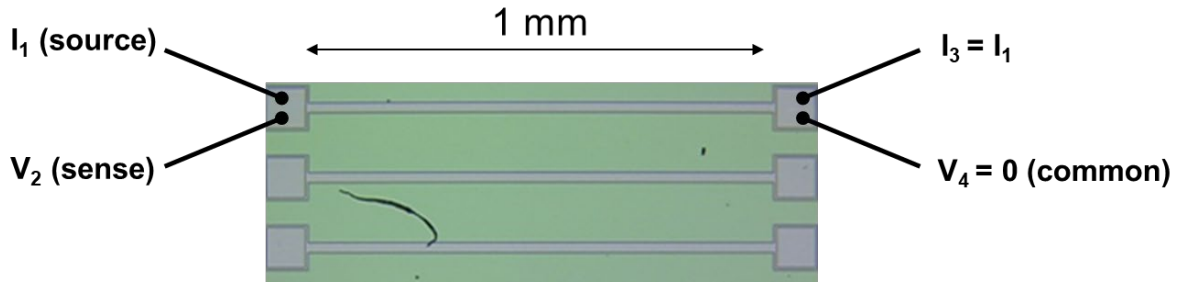

Figure 3. Diagram of the four-point probe measurement.

2.2.3 Radiation exposures

The devices were mounted to circuit boards and exposed to 0.5, 1, and 3 Mrad(Si) using a Co-60 gamma radiation source at the NASA JPL in Pasadena California. Radiation dose rate from the Co-60 source is dependent on distance from the source. For our experiments the samples were placed approximately 10 inches from the source and the dose rate was 45.6 rad(Si)/second. Samples were also exposed to 64 MeV proton radiation at UC Davis Crocker Nuclear lab. Average dose rate for these samples was 922 rad(Si)/second with a proton fluence of 4.4×10^{13} protons/cm^2. However, the high energy protons induced significant radioactivity in the support structure preventing testing these devices after radiation exposure.

2.3 Results and discussion

Each sample die contained 24 resistors, 12 attached and 12 released. 10 die were tested including 4 control die that traveled with the die to be exposed, 3 die for gamma exposure, and 3 die for proton exposure. As mentioned above we were unable to measure the proton exposed die due to induced radiation in the support structure.

All attached resistors were free from any physical irregularities, while 10% of the released beams were damaged by the fabrication process. Another 10% of the released beams had significant resistance changes distributed across the control and exposed samples. These outliers were not included in the analysis below. Measurements before and after radiation were separated by several weeks due to the necessity of transporting the samples to and from JPL and UC Davis.

After gamma radiation exposure, no visible changes were observed except for a discoloration of the circuit boards used to mount the die. Figure 4 (a) and (b) show a graph of the measured resistance changes for attached and released resistors, respectively. Although there does appear to be a dose dependent reduction in resistance, the change is very small at less than a half percent even at the highest dose and only the change at 3Mrad(Si) is statistically significant with $p < 0.001$.

These measurements indicate that there are few lasting effects of gamma radiation on the polysilicon MEMS platform. Future experiments measuring resistance changes immediately before, during, and immediately after radiation exposure would be of interest. In addition, measurements with lower energy protons would allow for determining any difference in radiation effects between proton and gamma radiation.

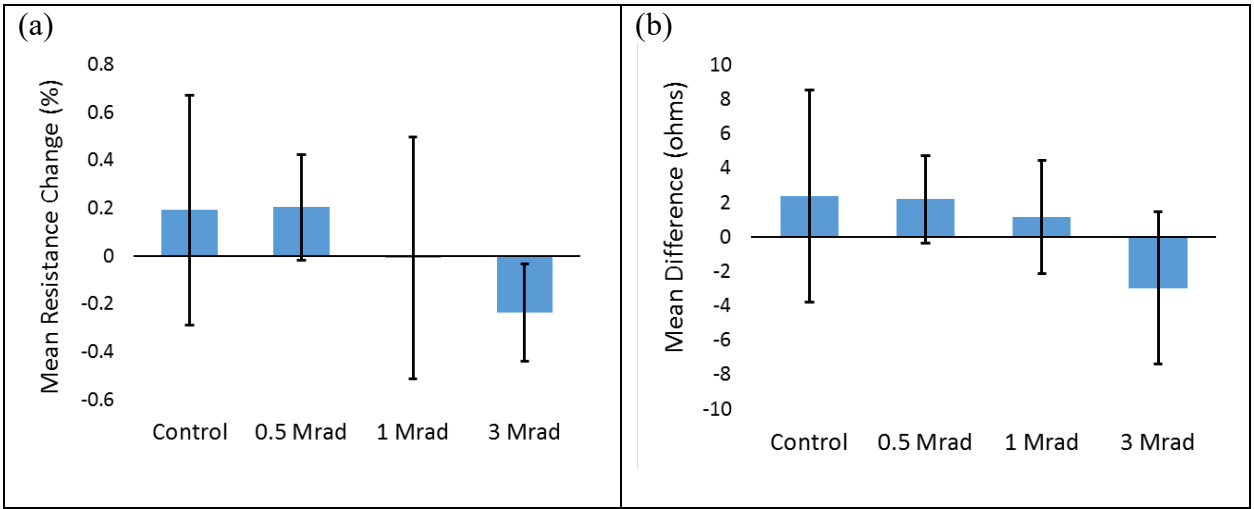

Figure 4: Plot of the resistance change for attached (a) and released (b) resistors. Error bars indicate standard deviation.

3 Comparing field emission performance of carbon nanostructures

3.1 Introduction

A practical requirement for an integrated vacuum circuit platform is the development of cathodes with high current density and long lifetime. Cold cathodes based on field emission from carbon nanostructures such as carbon nanotubes (CNTs) offer an attractive option because they avoid the thermal management issues of thermionic cathodes, which complicate miniaturization. CNT emitters in particular are well-suited for integrated MEMS vacuum microelectronics because they can be deposited or grown *in situ* in a variety of physical configurations. CNT cathodes have been demonstrated in a variety of devices with high emission levels, long lifetimes, and low fields (Figure 5) [10-12].

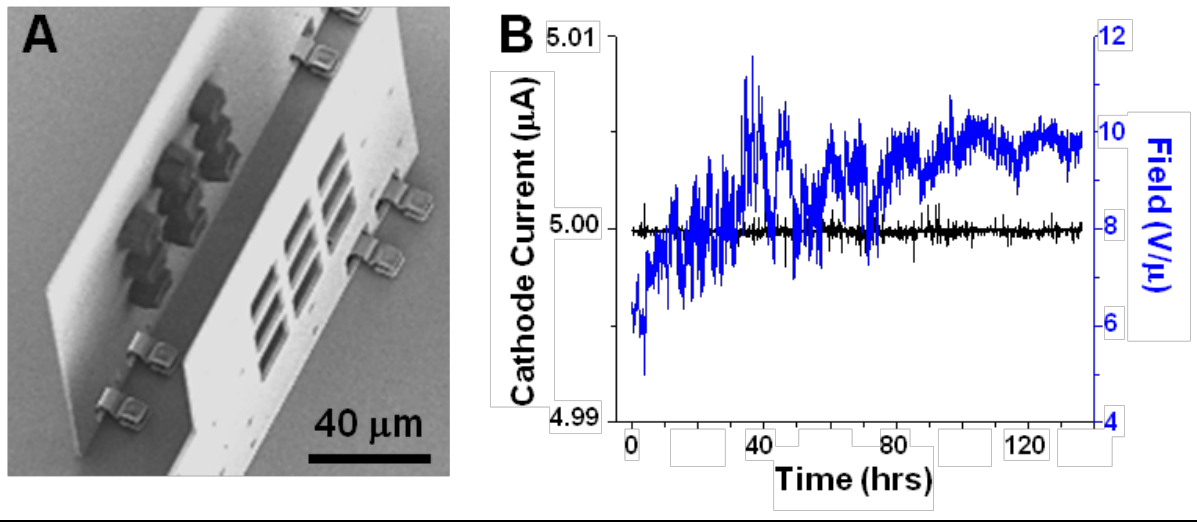

Figure 5. SEM image of a cathode and grid with a 3x3 array of CNT bundles (a). Plot showing 5 μA of cathode current sustained for over 130 hours from a cathode of the configuration shown in (a), (b).

Carbon nanostructures can be grown in a wide variety of morphologies ranging from basal plane textured highly oriented pyrolytic graphite ($HOPG_B$), textured fibers, nano-sheets, edge-textured highly oriented pyrolytic graphite ($HOPG_E$), activated carbon, aligned CNTs, bamboo CNTs (bCNT), graphenated CNTs, and aligned-graphenated CNTs. The different types are mainly classified according to dimensionality and edge density [13]. In particular, aligned-graphenated CNTs are an attractive morphology for field emission because they combine the high aspect ratio of aligned CNTs for increased field enhancement at the tips with increased edge density providing more field emission sites [12, 14].

In this section, we evaluated the field emission performance of three types of carbon nanotubes: aligned CNTs, graphenated CNTs, and aligned-graphenated CNTs. Results showed that the graphenated CNTs did not emit current at the fields applied, while the aligned CNTs performed better than the aligned-graphenated CNTs due to reduced electric field shielding.

3.2 Materials and methods

3.2.1 CNT growth

All CNTs are grown using a 915 MHz microwave plasma enhanced chemical vapor deposition (MPECVD) system with plasma power of 2150 W. Details of this system have been published by Cui et. al. [15]. All CNTs for these experiments are grown on arsenic doped n-type conductive Si substrates that have 5 nm thick Fe catalyst deposited using a CHA electron beam evaporation system. A shadow mask with 1.5 mm diameter holes was used to pattern the iron catalyst, resulting in 1.5 mm in diameter CNT films after growth. Achieving the different morphologies involves changing the temperature of the growth [13]. Below, the specific growth recipes for each sample type are described. Representative SEM images are shown in Figure 6.

3.2.1.1 Aligned CNTs

Aligned CNTs were grown at a reactor temperature of 850 ºC. The growth process consists of a heat-up step, during which ammonia flows into the growth chamber at a rate of 100 standard cubic centimeters per minute (sccm) and the chamber pressure increases to 21 Torr. When the chamber reaches 850 ºC, which takes approximately 180 seconds, a microwave plasma is struck while ammonia continues to flow at a rate of 100 sccm. The substrate is pretreated in the ammonia plasma for 120 seconds. This pretreatment step dewets the Fe catalyst film into nanoparticles of approximately 50 nm in diameter. After pretreatment, the growth stage begins as methane is introduced at a rate of 150 sccm and the ammonia flow rate is reduced to 50 sccm. The growth stage takes 180 seconds after which point the plasma, gas flow, and heating are turned off to end CNT growth.

3.2.1.2 Graphenated CNTs

Graphenated CNTs are grown using the same method at aligned CNTs, but at a higher temperature of 1050 ºC and the growth time is increased to 360 seconds [13].

3.2.1.3 Aligned-graphenated CNTs

Aligned-graphenated tubes are grown using a hybrid of the previous two growth processes. First aligned CNTs are grown at 850 ºC for 180 seconds using a 3:1 ratio of methane to ammonia as described in the growth process above. After the tubes have grown, the gas ratio remains the same and the temperature is increased to 1050 ºC for 120 seconds to induce graphenation [13].

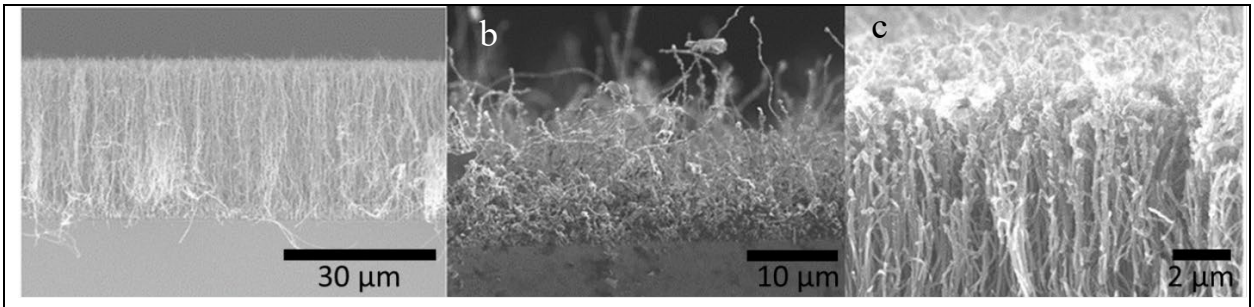

Figure 6. SEM images of aligned CNTs (a), graphenated CNTs (b), and aligned-graphenated CNTs (c)

3.2.2 Field emission characterization

Field emission characterization was done in a vacuum chamber at a pressure of approximately $1x10^{-6}$ Torr. A sample probe, shown in Figure 7, was built to facilitate the field emission experiments. It holds the sample in place and maintains a constant distance between the CNT cathode and the stainless-steel anode. The distance between the probe and the substrate was determined using SEM, as shown in Figure 8. Measured distance varied between 300-330 µm for different samples.

Electronic testing was done using two LabView controlled Keithley 2410 source measure units, one of which controlled the cathode voltage, and the other controlled the anode voltage. For all tests the cathode was held at 0 V, and the anode was swept from 0-1000 V, which corresponds to a field of up to 3.33 V/µm depending on sample-to-probe distance, while recording the current on each electrode. Due to small differences in probe-sample distance between samples, field emission analysis was conducted in terms of applied field, rather than applied voltage. To characterize the field emission current from each sample, ten voltage sweeps were conducted on each sample and the results from each of the ten sweeps were averaged together.

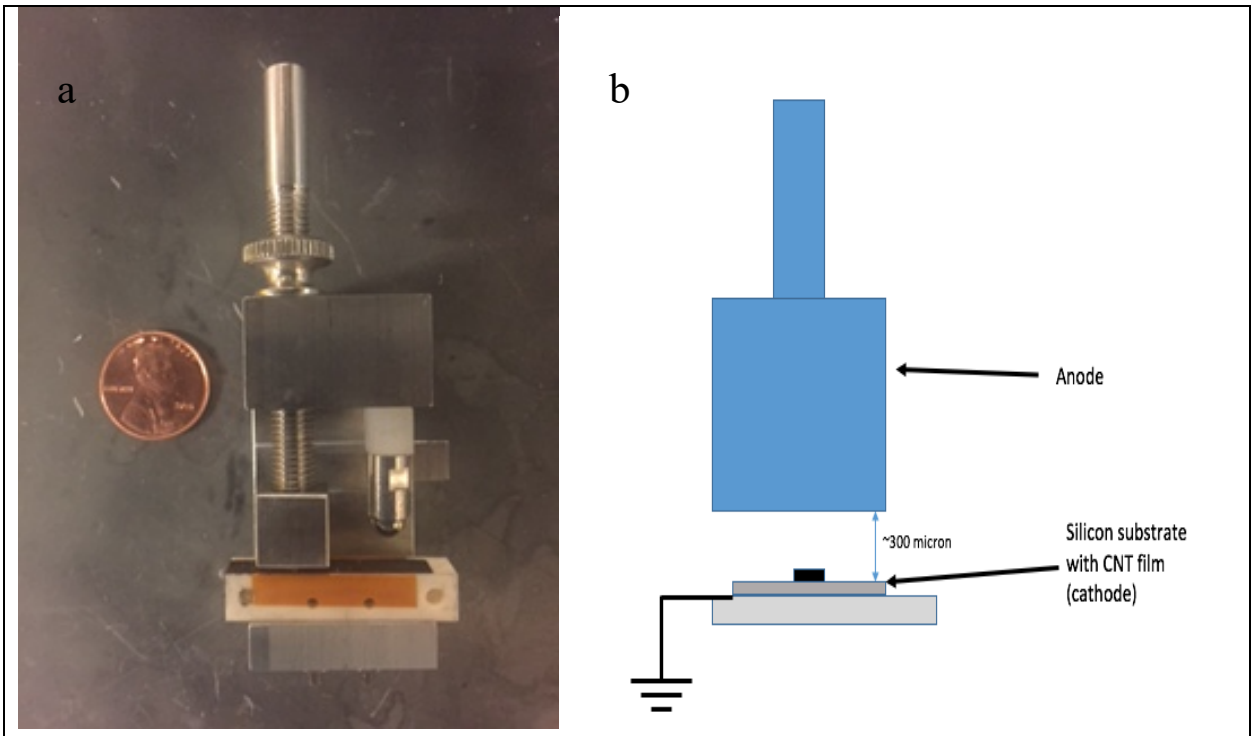

Figure 7: Image (a) and schematic (b) of the field emission probe setup. A penny is included in the image to indicate relative size.

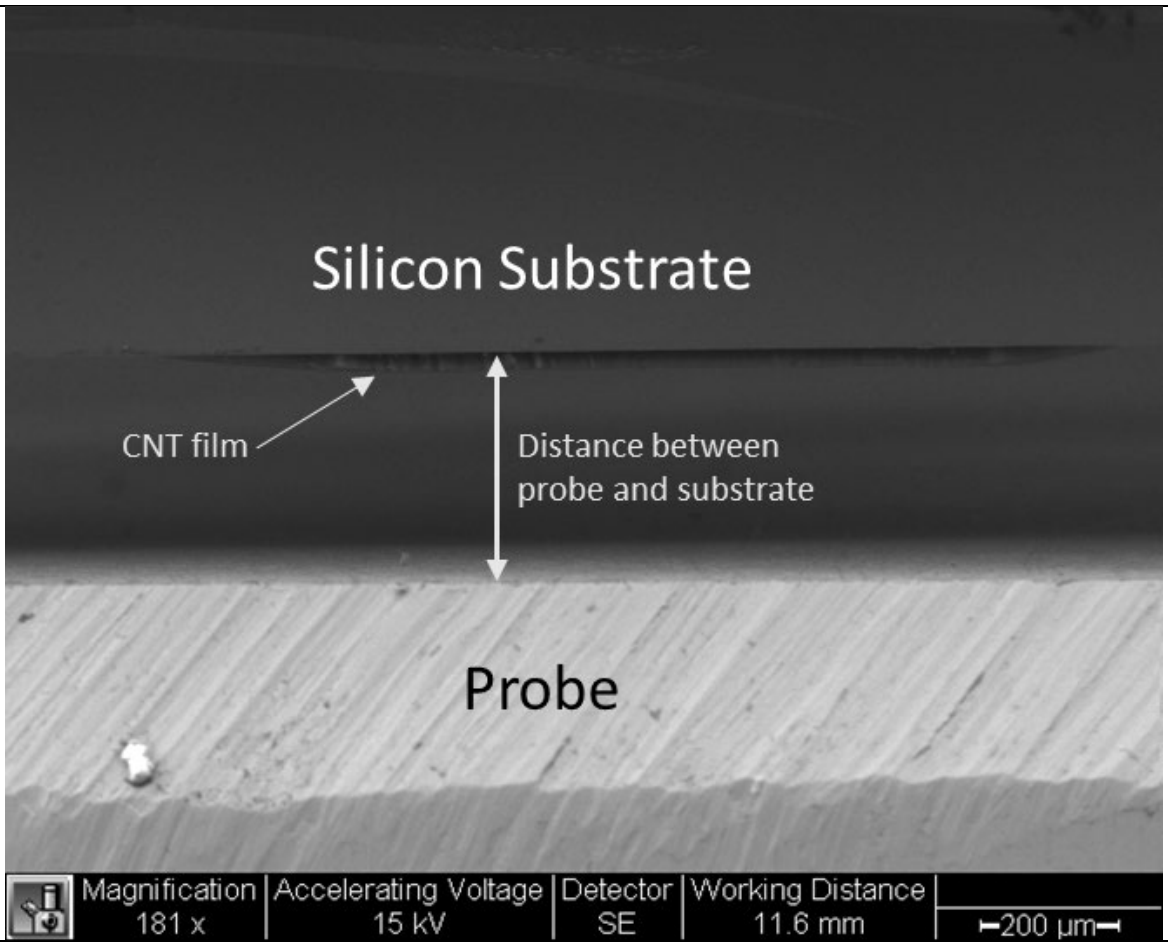

Figure 8: SEM showing CNT film and the distance between probe and silicon substrate

3.3 Results and discussion

The field emission performance of the three different samples were compared by measuring the turn-on field, defined as the field required to produce $1x10^{-9}$ A of current, and measuring the current density at 2.5 V/µm. The turn-on field was chosen as the field required to achieve emission of $1x10^{-9}$ A, as that is the smallest current that the Keithley 2410 can reproducibly measure.

No field emission was observed from the unaligned graphenated CNT sample while Figure 9 shows the field emission performance of the aligned CNT and aligned-graphenated CNT samples. Measured uncertainty, shown in green, represents standard deviation between the 10 scans that were averaged together. Both the aligned CNT and aligned-graphenated CNT samples show significant variability in the field emission performance as shown by the large standard deviation in the current at an applied field. This variability is due to work function changes at the CNT surface induced by adsorption and desorption of residual gas in the vacuum chamber. These work function changes result in fluctuation of the emission current [14, 16, 17]. For the aligned CNT sample (Figure 9 (a)), the turn-on field was 1.6 V/µm. This is typical for aligned CNT field emitter and performance is comparable to other results reported in literature [14, 18, 19]. With an applied field of 2.5 V/µm emission current density was $5.0x10^{-4}$ A/cm^2. For the

aligned-graphenated CNT sample (Figure 9 (b)), the turn-on field for this sample was 1.3 V/µm, and at an applied field of 2.5 V/µm the emission current was 6.0×10^{-5} A/cm^2.

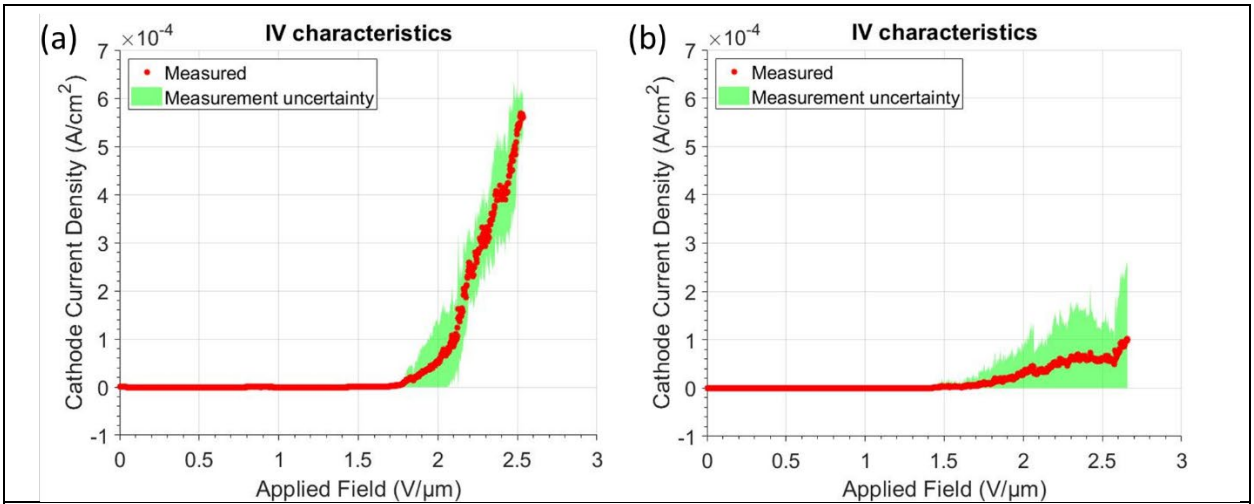

Figure 9. Comparing field emission performance of aligned CNTs (a) to aligned-graphenated CNTs (b)

The lack of field emission from the graphenated CNTs at the fields applied in this experiment is likely due to the unorganized orientation of the CNTs, as seen in Figure 6 (b). Literature has shown that when emitters are not parallel to the applied field, field enhancement factor is reduced [20]. The graphenation of the tubes also increases the individual tube width, which reduces the aspect ratio and field enhancement at the tip of the nanotube. The inverse relationship between emitter width and field enhancement factor has been reported in literature [18, 20].

Despite the lower turn-on field for the aligned-graphenated CNTs, the current density was much lower than for the aligned CNTs. This is contrary to reports in literature where field emitters with lower turn-on field typically have higher current density [21-23]. A potential explanation for this could be that in this sample there are some aligned-graphenated CNTs that are significantly longer than average leading to a lower turn-on voltage for these longer tubes.

Based on these results, we decided to focus on aligned CNTs for radiation exposures because lower turn-on field is not advantageous when it comes at the cost of significant reduction in current density.

4 The effects of gamma and proton radiation on aligned CNT field emitters

4.1 Introduction

Electron field emission is the quantum-mechanical phenomenon of electron tunneling through a surface potential barrier into vacuum in the presence of a sufficiently high electrostatic field. In contrast to thermionic emission and photoemission, field emission is the result of electrons tunneling through a reduced barrier rather than overcoming it energetically. In the absence of an applied electrostatic field the energy barrier for an electron at the conductor surface to reach vacuum is approximately rectangular. As seen in Figure 10 (a), by applying an electrostatic field at the surface of the conductor, the barrier becomes triangular allowing for electron tunneling. As

the field magnitude increases, the barrier narrows and tunneling current increases. Fowler and Nordheim developed a model for field emission where the emitted current, *I*, is a function of the material work function φ, and the field at the surface of the emitter *F:*

Equation 1: $$I = aF^2 e^{-\frac{b\varphi^{3/2}}{F}}$$

where *a* and *b* are constants [24].

In order to induce field emission from a planar cathode, an electric field on the order of $1x10^3$ V/μm is necessary to produce a sufficiently small tunneling barrier. However, by changing the morphology of the cathode to a sharp tip, the necessary applied field is greatly reduced. This can be incorporated into the model by introducing a field enhancement factor, β. $F = \beta E$, where *E* is the applied electric field [25]. The field enhancement phenomenon is due to concentration of the equipotential field lines around the sharp tip, as seen in Figure 10 (b). β increases in magnitude with increasing emitter aspect ratio [12, 26]. While planar emitters require an applied field of $\sim 10^3$ V/μm to induce emission, emitters with a high aspect ratio, such as CNTs, are capable of emitting in applied fields as low as 1 V/μm [27, 28] making them attractive for field emission applications.

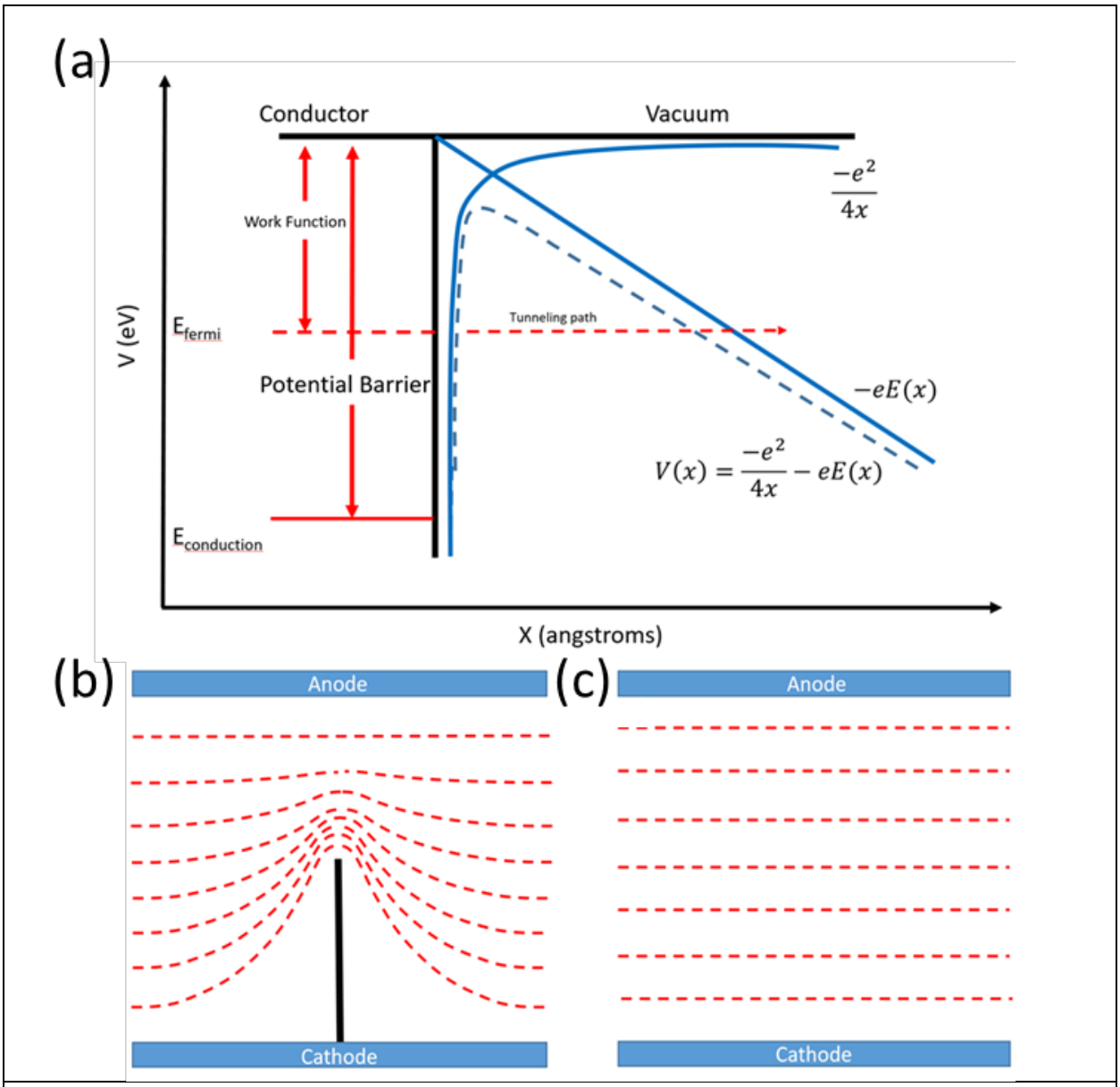

Figure 10: Diagram of how the triangular tunneling barrier is formed during Fowler-Nordheim emission with an applied electrostatic field (a). E is the magnitude of applied field, *V* is the electron potential energy and *x* is the distance away from the conductor surface. Equipotential field lines showing field enhancement at the tip of a high aspect ratio cathode (b), vs a planar cathode (c).

In addition to their attractive field emission properties, the robust material properties of CNTs make them a great potential candidate for use as field emission sources in high radiation environments, as they retain their structure even after exposure to high doses of radiation [29-31]. However, there has been no work done to characterize to the effects of proton and gamma radiation on aligned multi-walled CNT field emission performance.

This work investigates the effects of gamma and proton radiation on the field emission properties of aligned multi-walled CNTs grown by MPECVD before, during, and after radiation exposure. We do this by exposing CNT films to either gamma or proton radiation and characterizing their field emission performance before and after radiation using SEM and Raman analysis to correlate field emission changes to microstructural changes in the CNTs. We also study the effects of gamma radiation during CNT field emission by measuring the changes in voltage necessary to maintain a constant emission current with and without radiation present. Results show that gamma and proton radiation both decrease the defect density in CNTs, as measured with Raman spectroscopy, and this contributes to increased turn-on field in the samples. We did not observe any other effects of radiation on aligned CNT field emission performance. *in situ* characterization of field emission during gamma radiation exposure shows gamma radiation had no observable effect on the aligned CNT field emission performance.

4.2 Materials and methods

4.2.1 CNT sample preparation

Aligned CNTs were grown using the MPECVD growth process described in subsection 3.2.1 of this report. However, instead of catalyst spots with 1.5 mm diameter as were used in section 3, the iron catalyst was deposited through a photomask in spots of 100 µm, as shown in Figure 11. The reason for the smaller spot size is discussed below in subsection 4.3.2.1.

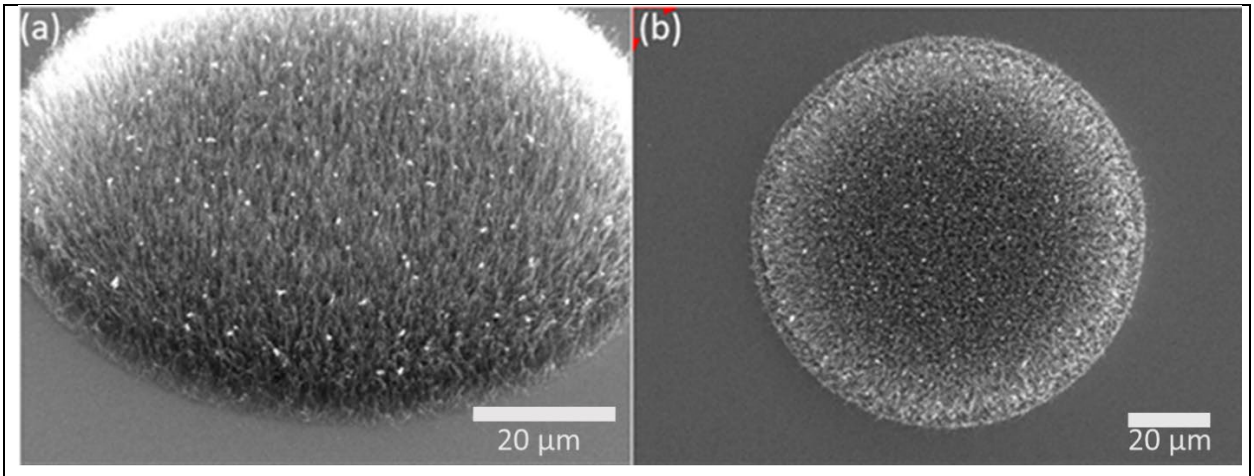

Figure 11: SEM of a representative sample of CNTs using 100 µm spot-patterned catalyst. In (a) the image is taken at a 45° angle and (b) shows the CNT spot from the top down

4.2.2 Sample characterization

4.2.2.1 SEM

An FEI XL-30 SEM was used to characterize the morphology of the CNTs before and after radiation exposure. We characterized the film morphology using magnification of 10,000x and 25,000x and surface morphology of the samples exposed to gamma radiation was done at 200,000x. For the samples exposed to gamma radiation we imaged the exact same area of the sample, and even the same specific CNTs to determine the effects of gamma radiation.

4.2.2.2 Raman

Raman spectroscopy was used to examine changes in defect density of the CNTs. The instrument used was a Horiba Jobin Yvon LabRam ARAMIS Raman spectrometer using a 633 nm laser. Because there is natural variation in defects across the CNT film, Raman data was taken at nine different spots across each sample, as shown in Figure 12. After irradiation, Raman characterization was done on the same nine spots for each sample.

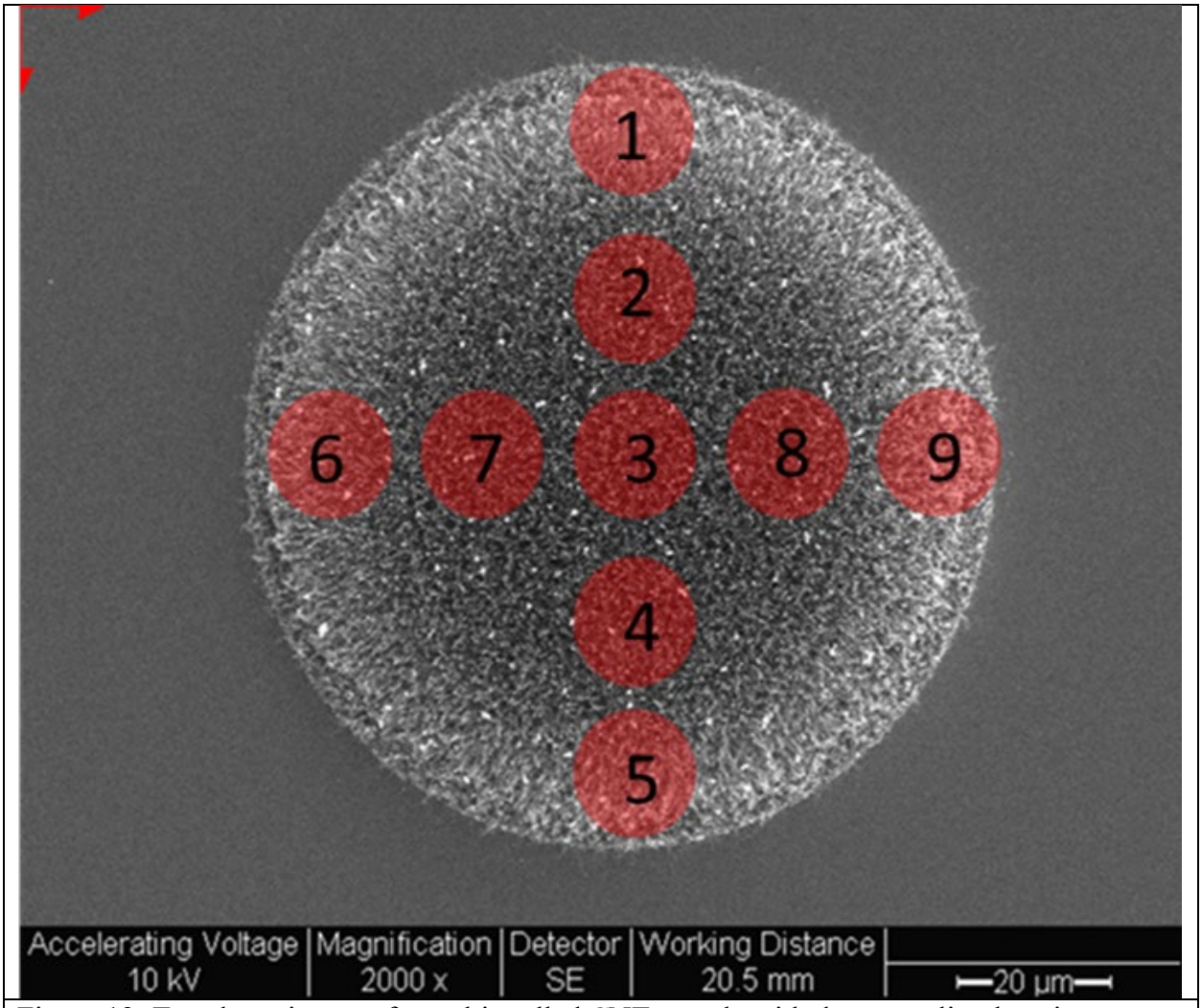

Figure 12: Top-down image of a multi-walled CNT sample with data sampling locations superimposed over the image. Each red spot represents the approximate area sampled by the Raman laser.

4.2.3 Radiation exposure

4.2.3.1 Gamma radiation

Gamma radiation exposure was conducted at the NASA JPL using a Cobalt-60 radiation source. Samples were irradiated at room temperature at atmospheric pressure. The dose rate was 45.6 rad(Si)/second and samples were exposed to TIDs of 0.5, 1, and 3 Mrad(Si).

4.2.3.2 Proton radiation

Proton radiation was conducted at the Crocker Nuclear Laboratory at the University of California at Davis. Samples were irradiated at room temperature. TID levels for proton radiation were 5, 6, and 8 Mrad(Si) using 64 MeV protons with an average dose rate of 922 rad(Si)/second with a fluence of 4.4×10^{13} protons/cm^2.

4.2.4 Field emission characterization

Field emission characterization was done in a vacuum chamber at a pressure of approximately 1×10^{-6} Torr. A sample holder, shown in Figure 7 (b) in subsection 3.2.2, was built to facilitate the field emission experiments. It holds the sample in place and maintains a constant distance between the CNT cathode and the stainless-steel anode. The distance between the probe and the substrate was determined using SEM. Measured distance varied between 100-300 µm for different samples.

Electronic testing was done using two LabView-controlled Keithley 2410 source measure units, one of which controlled the cathode voltage, and the other controlled the anode voltage. For all tests the cathode was held at 0 V, and the anode was swept from 0-1000 V while recording the current on each electrode. Due to differences in probe-sample distance between samples, field emission analysis was conducted in terms of applied field, rather than applied voltage. To characterize the field emission current from each sample, ten voltage sweeps were conducted on each sample and the results from each of the ten sweeps were averaged together.

4.2.5 *in situ* gamma radiation experiments

For *in situ* characterization of CNT field emission performance during gamma irradiation we designed and fabricated polysilicon MEMS vacuum microelectronic devices using CNTs as field emitters. These devices consist of two panels with a CNT-coated cathode and planar anode separated by a gap of 35 µm. SEM images of a two-panel device are shown in Figure 13. Fabrication of these devices was done using the same PolyMUMPs process as the MEMS NOR gates devices described in subsection 5.2 of this report [2].

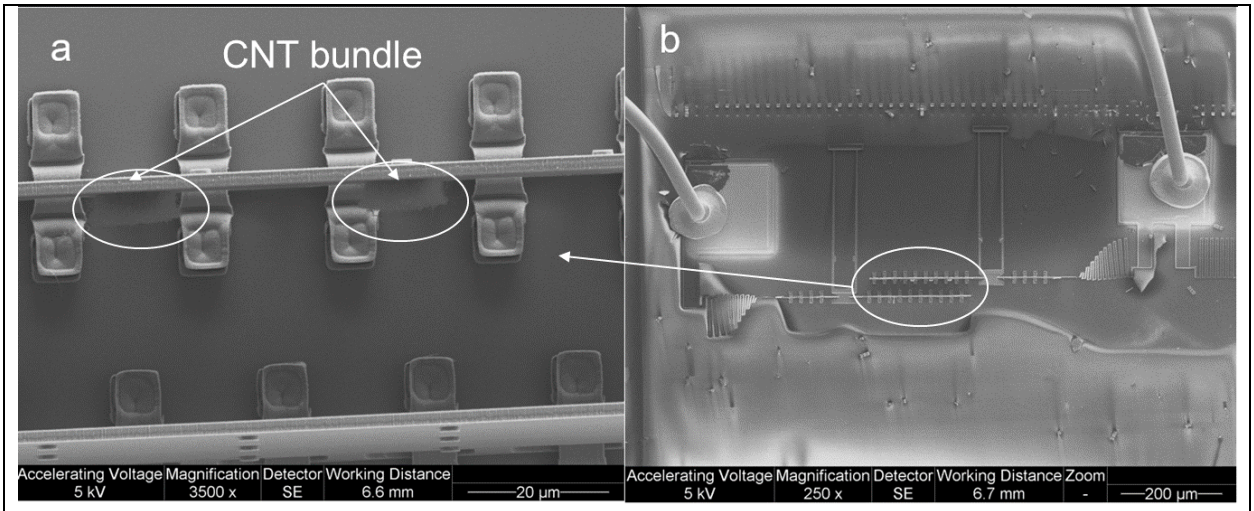

Figure 13: SEM images of a two-panel device with CNT cathode and planar anode. (a) is a magnified view of the circled area in (b).

Gamma radiation exposure for *in situ* testing was done at NASA's Jet Propulsion Lab using a cobalt-60 source. Devices were tested into a vacuum chamber evacuated to $1x10^{-3}$ Torr which was placed in front of the Co-60 source. A lower pressure would have been preferable, but the necessity of placing the vacuum pumps behind a radiation shield required use of a long tube between the vacuum pump and vacuum chamber. The low conductance of the 2-meter-long tube limited the base pressure inside the vacuum chamber. The 45.6 rad(Si)/second source was cycled on and off with a period of approximately 5 minutes while the potential difference between the cathode and anode was varied to maintain a constant current. For these experiments, cathode currents of $1x10^{-8}$ A and $5x10^{-8}$ A were analyzed. Performance with and without radiation was evaluated by comparing the required variation in potential difference to maintain a constant current. Two devices were tested in this manner.

4.3 Results

4.3.1 SEM analysis before and after radiation exposure

Figure 14 shows SEM images before and after 3 Mrad(Si) gamma irradiation and Figure 15 shows SEM images before and after 8 Mrad(Si) proton exposure. Analysis of the images show no observable effects of either gamma or proton radiation on the CNT morphology. Figure 14 (a) and (b) show a CNT film and a single CNT, respectively, before gamma radiation exposure, and (c) and (d) show the exact same areas of the sample after a TID of 3 Mrad(Si) gamma irradiation. SEM analysis shows that the gamma radiation had no effect on the structure of the film or on the surface structure of the CNTs themselves. The results from proton irradiation, shown in Figure 15 similarly show no change in CNT structure.

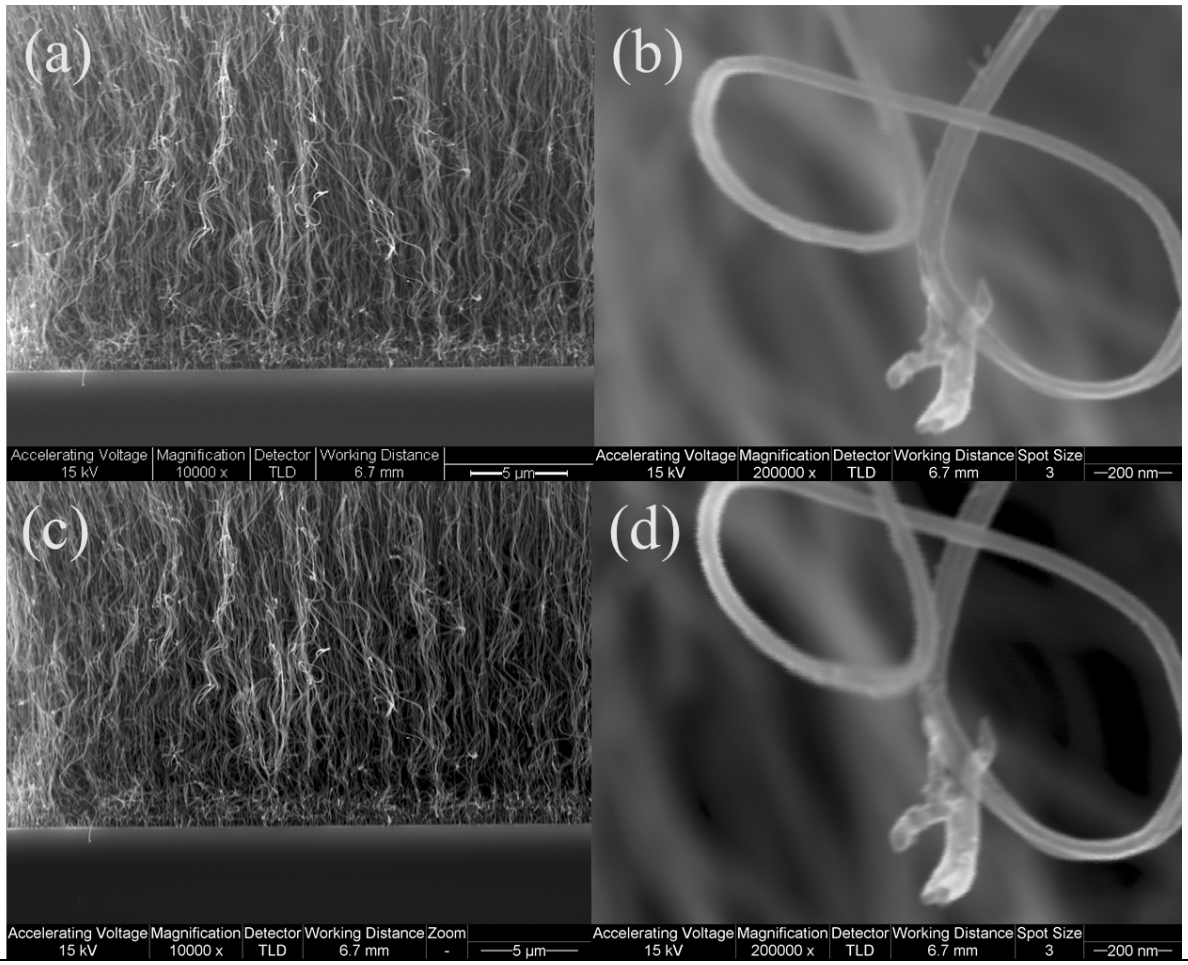

Figure 14: images (a) and (b) show the CNTs before gamma radiation and (c) and (d) show the same CNTs after 3 Mrad(Si) gamma radiation exposure

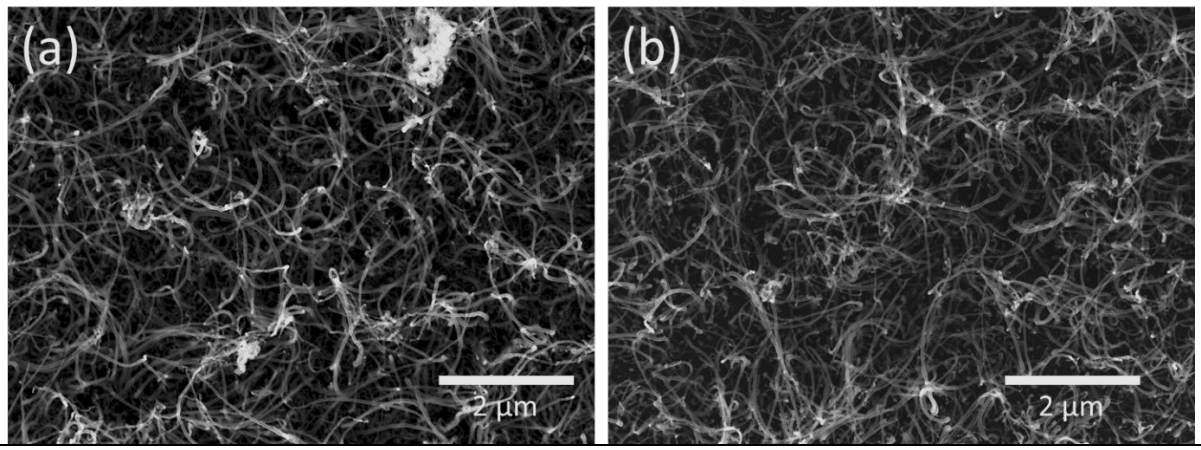

Figure 15: CNTs before (a) and after (b) 8 Mrad(Si) proton irradiation

4.3.2 Raman spectral analysis

4.3.2.1 Spatial variation in Raman spectra across the CNT film

Raman characterization is an established tool for analyzing defect density in CNTs, particularly single-walled CNT (SWCNT) films. [32]. Raman analysis of multi-walled CNT films, however, is not as straightforward due to variations in tube diameter and tube structure that are observed experimentally [32, 33]. We observed this in our own work when initially trying to use Raman to characterize defect density of multi-walled CNT films 1.5 mm in diameter. Figure 16 shows how Raman D/G peak height ratio varies across a film 1.5 mm in diameter. Data was taken at 22 different locations across the sample and widely varying D/G peak height ratios were found. Standard deviation across the sample was 0.061 and the largest difference in D/G ratio between spots was 0.25. As changes in D/G ratio due to radiation are similar in magnitude, a method to measure Raman spectra on the same spot before and after radiation exposures is necessary. Therefore, we chose to decrease our film diameter from 1.5 mm to 100 µm. This brings our film diameter within one order of magnitude of the Raman laser spot size, which is approximately 10 µm, and allows us to sample the same spot on the sample before and after radiation treatment.

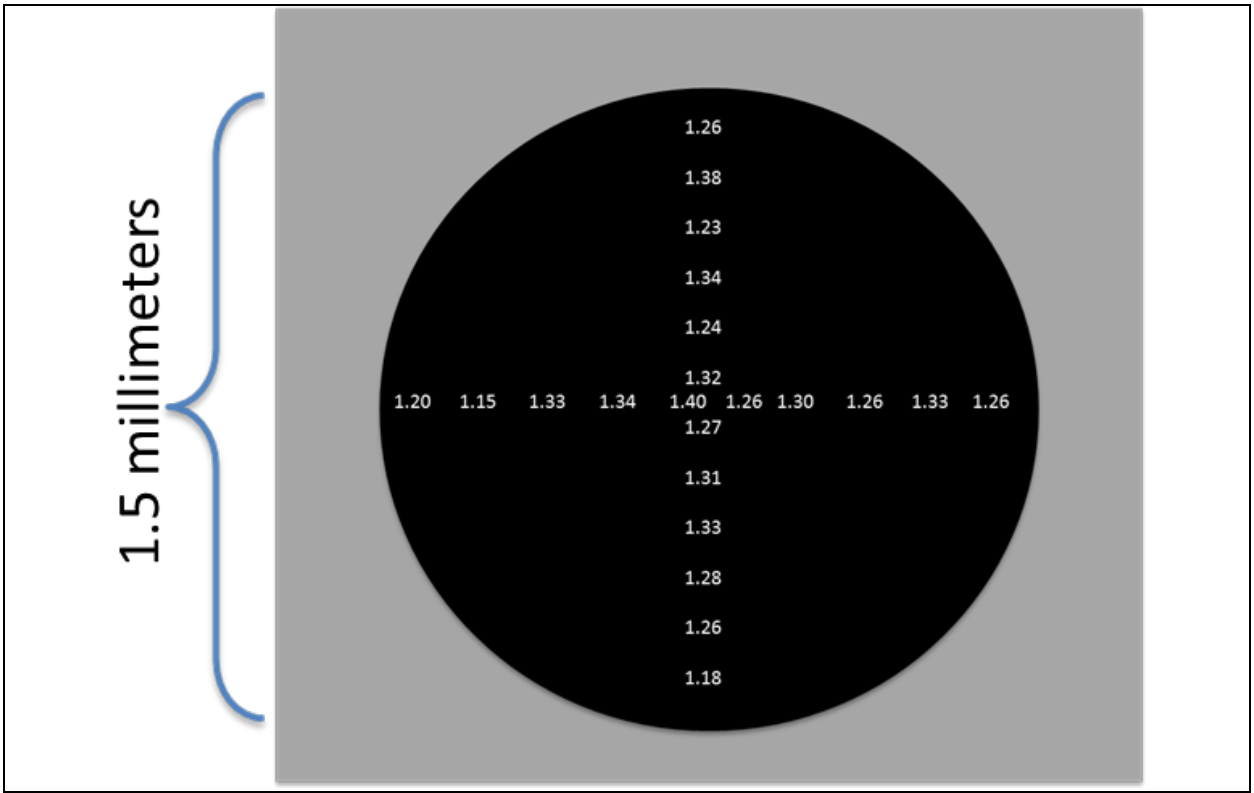

Figure 16: Schematic showing how Raman D/G peak height varies across a CNT film 1.5 mm in diameter. Data was taken at 22 different points across the sample. Each number represents the D/G peak height ratio taken at that location on the sample.

4.3.2.2 Raman spectral analysis before and after exposure to radiation

Figure 17 shows representative Raman spectra in the region of 1100 – 1800 cm^{-1}. The peak at 1325 cm^{-1} corresponds to the defect vibrational or D mode while the peak at 1572 cm^{-1} is the

graphitic or G vibrational mode. Literature indicates that a qualitative measure of the defect density of a CNT film can be obtained by the ratio of the D/G intensity [32, 34]. Table 1 shows the average D/G ratio for the 9 spots on each sample described in the method section before and after exposure to radiation. In all but one case, there is a small but statistically significant *decrease* in defect density as a result of radiation exposure.

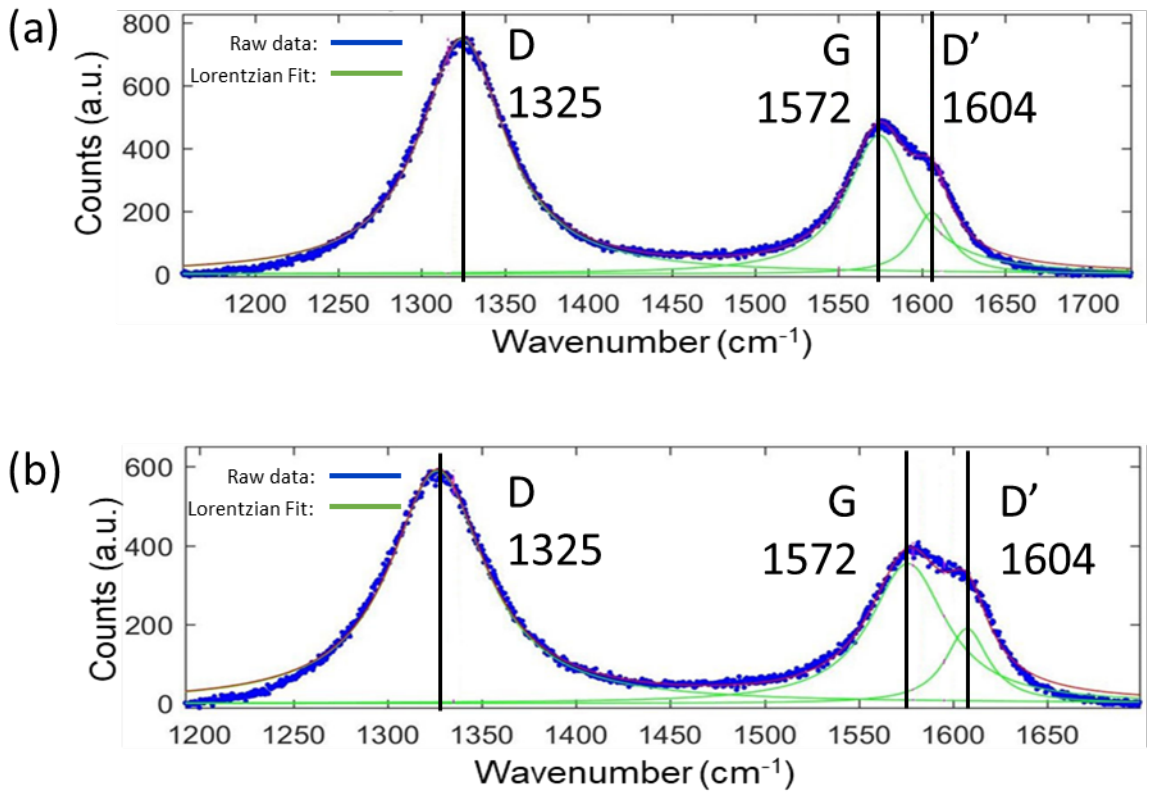

Figure 17. Representative Raman spectra before (a) and after radiation (b)

Table 1: changes in Raman D/G ratio for samples exposed to gamma and proton radiation

Sample	Irradiation (Mrad(Si))	Average D/G Ratio	Percent Change In D/G Ratio
NFQ140_1	0	1.88	
NFQ140_1	0.5 (1.17 MeV, 1.33 MeV γ)	1.76	**-7 (±1.5)**
NFQ135	0	1.59	
NFQ135	1 (1.17 MeV, 1.33 MeV γ)	1.41	**-11 (±1.6)**
NFQ85	0	1.7	
NFQ85	3 (1.17 MeV, 1.33 MeV γ)	1.67	**-2 (± 0.44)**
NFQ138	0	1.44	
NFQ138	0.5 (64 MeV proton)	1.4	**-3 (± 1.5)**

UNK1	0	1.45	
UNK1	6 (64 MeV proton)	1.18	**-18 (± 2.5)**
NFQ143	0	1.9	
NFQ143	6 (64 MeV proton)	1.74	**-8 (± 0.91)**
NFQ131_1	0	1.68	
NFQ131_1	8 (64 MeV proton)	1.72	**3 (± 2.0)**

4.3.3 Field emission performance

To evaluate the field emission performance before and after radiation exposure we measured the turn-on voltage and analyzed the IV curves according to the Fowler-Nordheim model described in subsection 4.1.

4.3.3.1 Turn-on voltage

We have defined the turn-on voltage is the field required to generate $1x10^{-9}$ A of emission current. We chose $1x10^{-9}$ A because this is the lowest value that our Keithley 2410 source measure unit can accurately measure. Table 2 is a table of the turn-on field for each sample before and after gamma or proton radiation. In all but one sample, the radiation resulted in an increase in turn-on field. Note that sample NFQ131_1 that shows a decrease in turn-on field also showed an increase in defect density (Table 1).

Table 2: changes in E_{to} for CNT samples before and after exposure to radiation

Sample	**Irradiation (Mrad(Si))**	**E_{to} (V/µm)**	**Change in E_{to} (V/µm)**
NFQ140_1	0	5.1	
NFQ140_1	0.5 (1.17 MeV, 1.33 MeV γ)	6.2	1.1
NFQ135	0	2.4	
NFQ135	1 (1.17 MeV, 1.33 MeV γ)	4.2	1.8
NFQ85	0	2.8	
NFQ85	3 (1.17 MeV, 1.33 MeV γ)	6.2	3.4
UNK1	0	2	
UNK1	5 (64 MeV proton)	2.5	0.5
TCR350_7	0	1.2	
TCR350_7	6 (64 MeV proton)	1.4	0.2
NFQ131_1	0	5.3	
NFQ131_1	8 (64 MeV proton)	3.3	-2

4.3.3.2 Fowler-Nordheim analysis

Change in field emission performance can be analyzed by determining the field enhancement factor, β, which is calculated using IV scan data to generate a Fowler-Nordheim plot in which $Ln(I/E^2)$ is plotted with respect to 1/E, as shown in Figure 18. β is determined by doing a linear fit of the data following device turn-on. As seen in Figure 18, some data sets had two distinct

slopes, and in these cases we obtained two values for β, referred to as β_1 and β_2. Other researchers have also observed multiple field enhancement factors CNT field emission and several theories have been presented [14, 35, 36]. One possible explanation is that as current density increases with field strength, joule heating of the CNTs leads to Schottky electron emission that contributes to the overall current [36].

Table 3 shows the calculated β_1 and β_2 values obtained from samples before and after radiation exposure. There is no apparent correlation between β_1 and β_2 before and after radiation exposure.

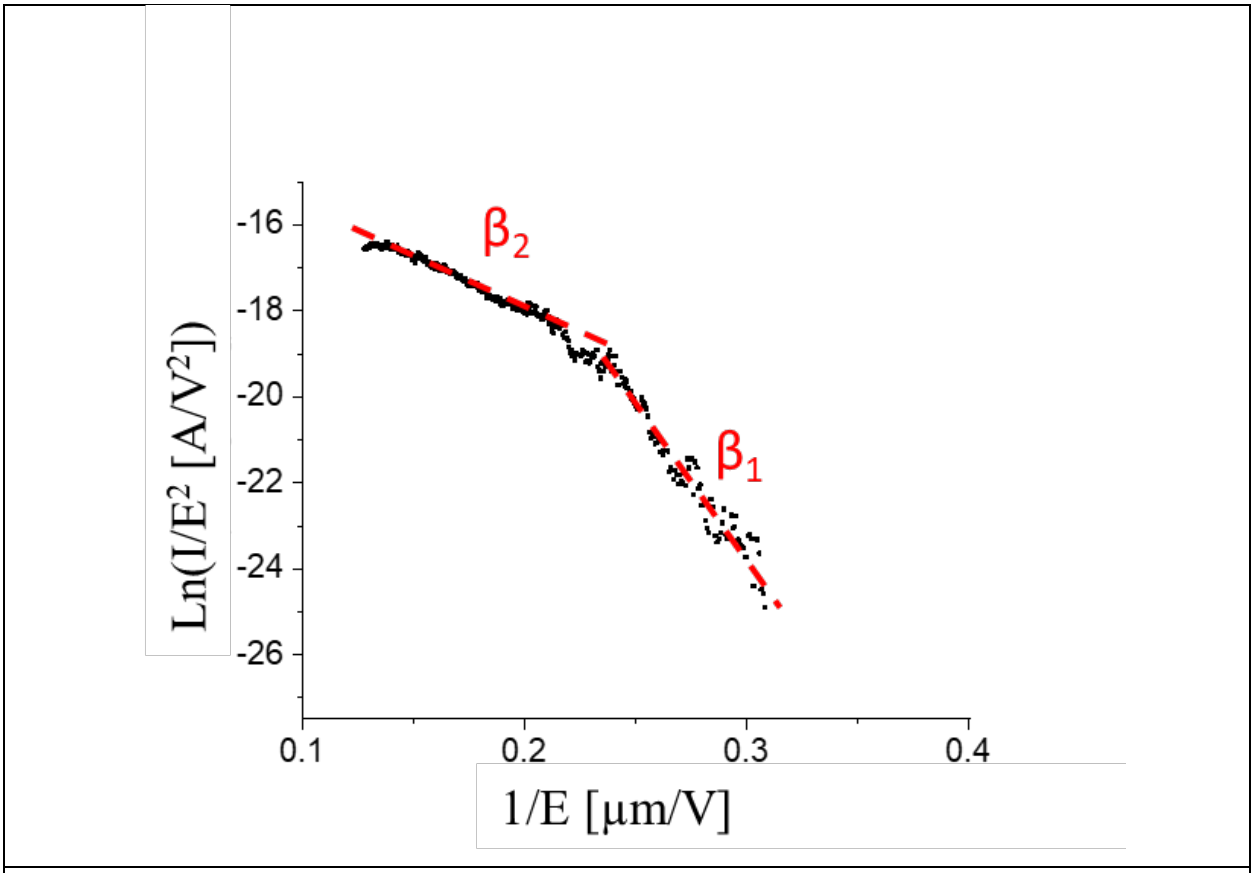

Figure 18: Example Fowler-Nordheim analysis with linear fits used to determine field enhancement factors β_1 and β_2

Table 3: Field enahancement factor for samples before and after exposure to radiation

Sample	**Irradiation (Mrad(Si))**	β_1	β_2
NFQ140_1	0	604	n/a
NFQ140_1	0.5 (1.17 MeV, 1.33 MeV γ)	1463	n/a
NFQ135	0	1294	3020

NFQ135	1 (1.17 MeV, 1.33 MeV γ)	997	n/a
NFQ85	0	1053	2991
NFQ85	3 (1.17 MeV, 1.33 MeV γ)	669	n/a
UNK1	0	2550	n/a
UNK1	5 (64 MeV proton)	1840	4580
TCR350_7	0	3880	8990
TCR350_7	6 (64 MeV proton)	1860	7370
NFQ131_1	0	745	n/a
NFQ131_1	8 (64 MeV proton)	1140	2950

4.3.4 *in situ* gamma radiation experiments

Figure 19 shows a plot of anode voltage for a representative two-panel device (see Figure 13) vs time. The anode voltage is varied to maintain a current set-point of either $1x10^{-8}$ A or $5x10^{-8}$ A. The voltage variation required to maintain a constant emission current is a result of localized work-function changes due to adsorbates and changes in CNT morphology and due to physical damage to the field emitters [14]. The sample was exposed to gamma radiation at approximately 5 minute intervals as shown by the green shading on the graph.

For an emission current of $1x10^{-8}$ A, while the overall magnitude of the voltage variation is similar when the radiation is on vs off, the rate of variation in voltage appears to be significantly less when the gamma radiation is on. To quantify the voltage variation, we took the standard deviation of the derivative of the anode voltage vs time, and indeed the rate of variation is significantly less when the radiation is on than when the radiation is off. However, for an emission current of $5x10^{-8}$ A, the rate of variation in voltage is roughly equivalent to the rate of variation when the radiation is off. A second device was also tested, which exhibited similar results.

A control experiment taken with similar conditions, but in the absence of field emission on a device with damaged carbon nanotubes, indicates that there is $7.7x10^{-9}$ A background current due to ionization of residual gas in the vacuum chamber by the gamma radiation, as shown in Figure 20. As this background current is similar in magnitude to the current set-point, it is likely the cause of the reduced voltage variation required to maintain a constant emission current of $1x10^{-8}$ A. At the higher emission current of $5x10^{-8}$ A the CNT field emission dominates the current at the anode, and the voltage variation required is similar with and without radiation.

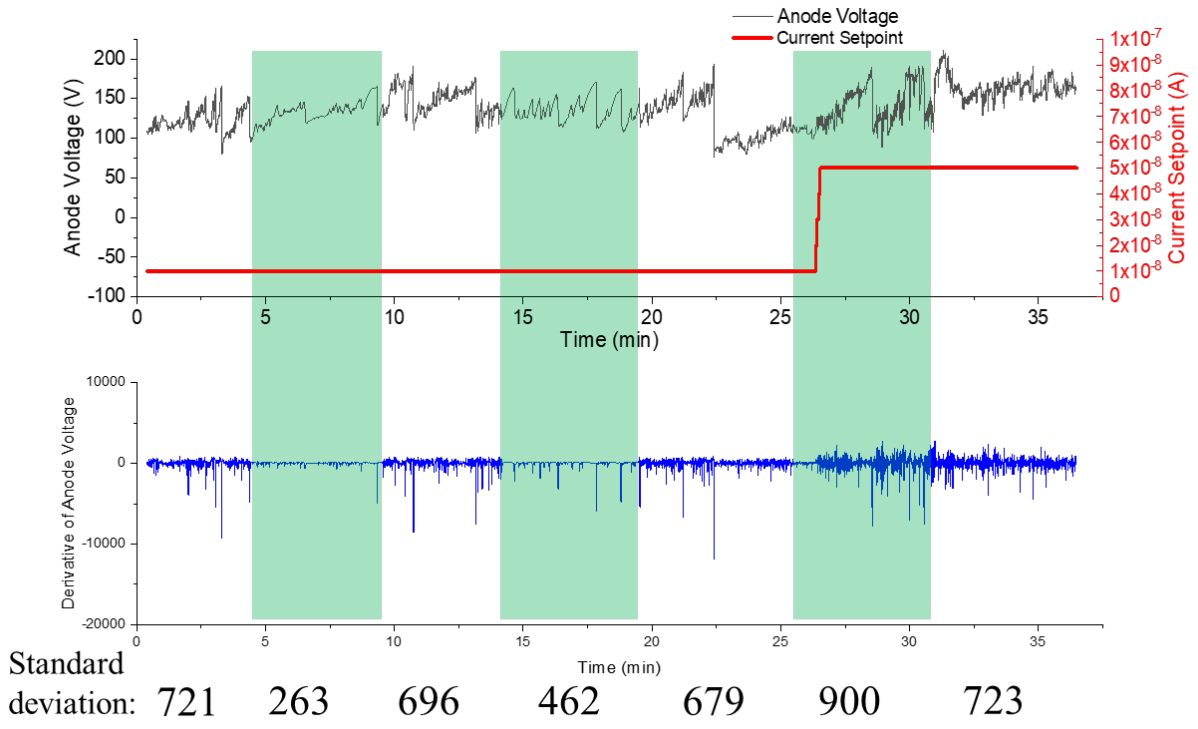

Figure 19: anode voltage and standard deviation of anode voltage for a two-panel device while radiation is switched on (green sections) and off (white sections).

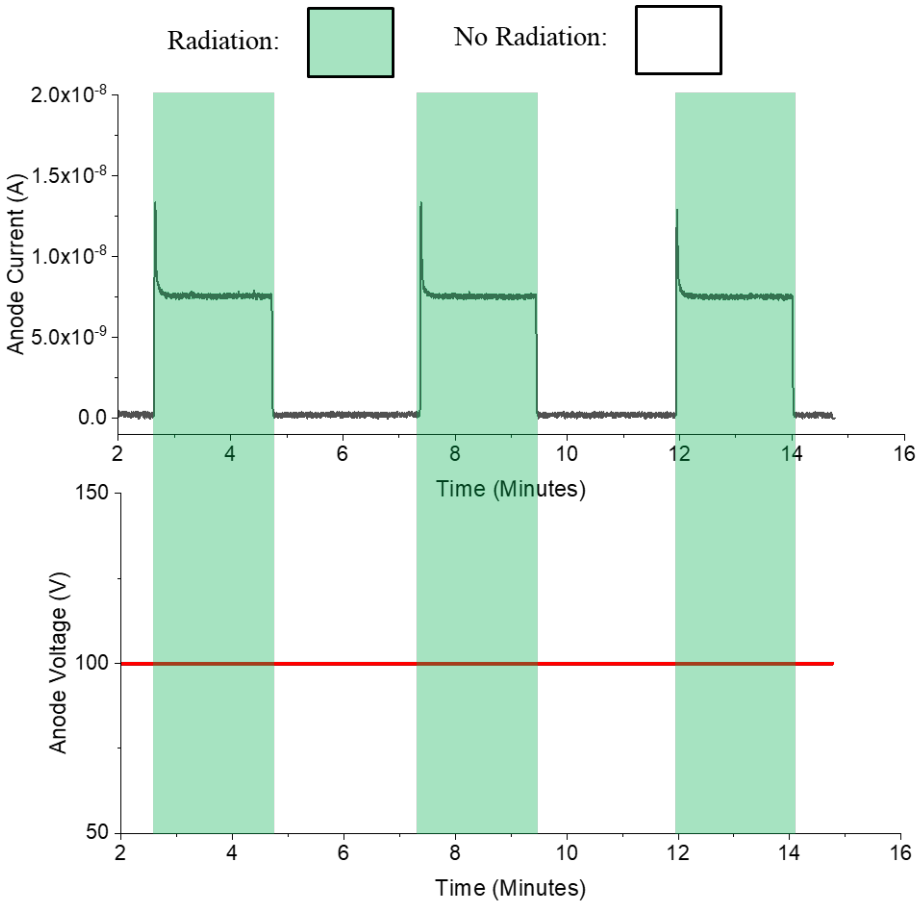

Figure 20: Anode current and voltage during radiation exposure (green) and without radiation exposure (white)

4.4 Discussion

The Raman results in Table 1 indicate that in most cases, both proton and gamma radiation alter the microstructure of the CNTs by reducing the defect density, as observed in the decrease in Raman D/G peak height ratio. The decrease in D/G ratio indicates an increase in sample order. Similar observations have been reported for graphite and diamond [37] and for CNTs [38]. This microstructural change leads to an increase in turn-on field for field emission – consistent with previous work conducted by Lee et. al., Patil et. al., and Kim et. al. which all showed increase in CNT defect density leading to reduction in CNT FE turn-on field [39-41]. Reduced defect density has a negative impact on field emission performance as CNTs have been shown to preferentially emit from defect sites [41]. The increase in turn-on field can be explained by the reduction in defect density in the CNT films, as CNTs with fewer defects have fewer emission sites.

While we observed a correlation between defect density, turn-on field, and radiation exposure described above, we were not able to discern any correlation between radiation and the field enhancement factor. The lack of correlation between field enhancement and radiation is likely

due to the large emission current fluctuations caused by adsorption and desorption of residual gases in the vacuum chamber altering the work function of the CNTs [14, 16, 17]. These large emission current fluctuations are likely masking any other effects due to radiation. The work function changes caused by adsorption and desorption of gases could also account for the variations we observed in field enhancement factor, β. β is determined by fitting the IV data to the Fowler-Nordheim equation (*Equation 1*), a constant work function for the emitter is assumed. Adsorption and desorption of gases change the localized work function of the CNTs during emission, and these changes affect the calculated value of β.

in situ measurements indicate that for low emission currents, the rate of change of voltage vs time required to maintain a constant emission current was less during radiation exposure than without radiation exposure. This is likely due to a similar order of magnitude background current from ionization of residual gas in the chamber by the gamma radiation. At higher emission currents, the field emission dominates, and the voltage variation required to maintain a constant emission current is similar with and without radiation.

In conclusion, exposure to radiation results in no observable physical damage to the CNTs at the radiation levels tested. However, small microstructural changes observed with Raman spectroscopy correlate to a reduction in defect density that leads to an increase in turn-on voltage for field emission. Adsorption and desorption of gasses on the surface of the CNTs resulting work function changes and emission current fluctuations mask other changes in field emission properties. Finally, *in situ* measurements indicate that for high enough currents, the voltage variation required to maintain a constant emission current is similar with and without radiation exposure.

5 Design, fabrication, and characterization of a polysilicon MEMS NOR gate vacuum microelectronic device with integrated CNT field emitters

5.1 Introduction

Since the invention of the transistor in 1949 solid-state technology has dominated the electronics industry [42]. Due to its low cost and scalable integration, solid-state electronics quickly replaced vacuum-based technologies for most applications. Despite the performance benefits of solid-state technology, there are still several applications for which they are not well suited, such as use in high radiation environments [43].

Vacuum microelectronics utilizing field emitters as electron sources are an alternative to solid state devices for use in extreme environments [44-48]. CNT-based field emitters have emerged as an improvement on Spindt emitter technology [49]. The fine nanostructure of CNTs enhances field emission and the robust nature of CNTs allows for current density greater than 13 A/cm^2 [50]. These properties make CNTs a promising material candidate for field emission devices [51].

Our group has been using an established process for micromachining polysilicon based MEMS devices, known as PolyMUMPs [2], to develop vacuum microelectronic devices with integrated CNT field emitters. Thus far we have demonstrated a variety of devices including triodes, ion

sources and a bipolar microelectronic device [3-5, 10, 52, 53]. This work demonstrates a vacuum microelectronic NOR logic gate using CNT field emitters, shown in Figure 21 (a). The device consists of two parallel vacuum tetrodes with a common cathode and a common anode and has a semiconductor analog that is shown in Figure 21 (b). The common cathode has two CNT field emitter arrays. CNT emission is independently controlled by an extraction grids, which are biased to extract electron current from the CNTs. Each side of the device has an independent stopping grid, which is biased to control the electron current flowing from the extraction grid to the anode. This work discusses the design, fabrication, and characterization of this device.

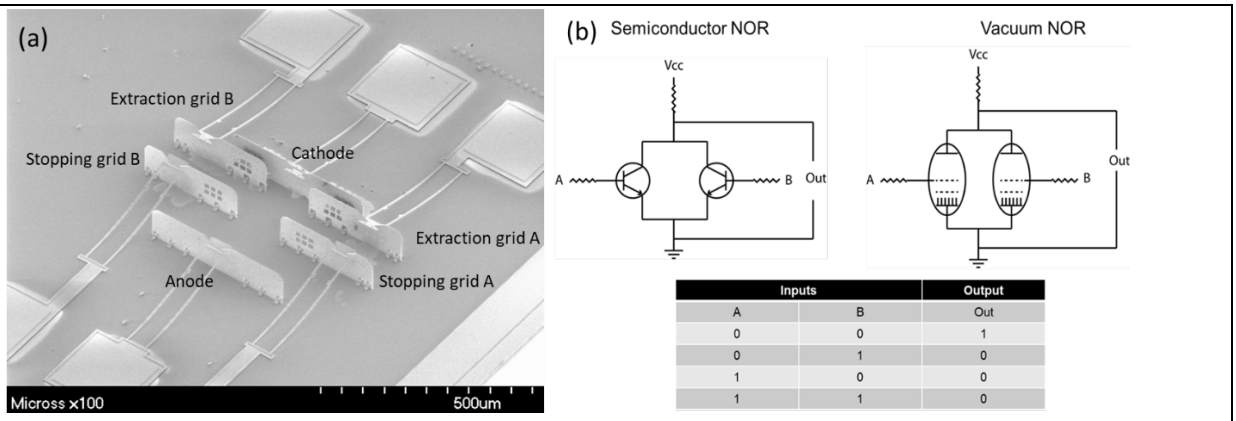

Figure 21: SEM image of a MEMS NOR gate with primary components labeled (a) and a schematic of the vacuum NOR gate compared to a semiconductor NOR gate (b).

5.2 Materials and methods

Polysilicon vacuum microelectronic devices were fabricated using a well-established polysilicon MEMS process known as PolyMUMPs. Details of the fabrication process have been described in previous publications [2, 52]. In brief, devices are fabricated by etching and micromachining a three-layer polysilicon substrate. Following the MEMS processing, a 5 nm thick layer of iron is evaporated through a photomask onto the cathode. This serves as a catalyst for CNT growth. Aligned CNTs are grown on the cathode using a microwave plasma chemical vapor deposition. CNTs are grown at 850 ºC using a 120 second ammonia catalyst pretreatment step, and a growth step with a 3:1 ratio of methane to ammonia for 180 seconds. Pressure throughout the growth process is 21 Torr. More details on the MPECVD growth process can be found in section 4 of this report. After CNT growth the panels are manually lifted perpendicular to the substrate and held in place with integrated latches. Each chip is then mounted and wire bonded to a pin-grid array.

Device performance characterization was done in vacuum at pressure of ~5×10^{-7} Torr using individual Keithley 2410 source meters to control voltage at each panel of the device. To characterize the field emission performance of the CNTs field emitters we sweep the voltage of the extraction grid from 0-150 V relative to the cathode. Distance between the cathode and extraction grid is 33 µm, so this corresponds to an applied field of 0-4.5 V/µm. To account for variation in the cathode current we conducted 10 sweeps and averaged them together.

Integrated device performance is characterized in two configurations. First, as a tetrode, in which only one side of the device operates. Second, as a NOR logic gate, in which both sides of the device are used. In the tetrode configuration we examine the switching capabilities of the device and transistor-like performance. The NOR configuration operates in a very similar way to a traditional semiconductor NOR logic gate, as shown in the schematic in Figure 21 (b). Electrons are extracted from the cathode by positively biasing the extraction grid relative to the cathode. Due to the noisy nature of CNT field emission, as described in Section 4, we use a hardware feedback loop in the Keithley 2410s that modifies the potential of each of the extraction grids to maintain a constant emission current from each side of the device.

5.3 Results and discussion

5.3.1 NOR gate and tetrode design

Figure 22 shows a 2-D electron trajectory simulation done with COMSOL of the NOR gate operation with one side on and the other side off. The figure shows the various components of the NOR gate and their relative positions. The device is symmetric about x = 0. The cathode at y = 0 has two sets of CNT emitters bundles on each side of the device. The CNT emitters are arranged as a 3 x 2 array of CNT patches 9 μm on a side and separated by 9 μm. Positioned 35 μm in front of the cathode are two independently controlled extraction grids with holes 14 x 14 μm centered above the CNT bundles. Then positioned 150 μm from the cathode are two independent stopping grids with holes 15 x 15 μm centered above the CNT bundles. Finally, a shared anode is positioned 300 μm from the cathode.

As shown in the simulated results, the extraction grids are used to generate field emission from the CNT bungles. The stopping grids of the device function as switches that either block or allow current to flow from the extraction grid to the anode, dependent on how they are biased. When potential is positive, electrons pass through the grid and the circuit between the cathode and anode is closed, when potential is negative, electrons are blocked from reaching the anode, leaving an open circuit. This mechanism is responsible for the NOR gate nature of our device.

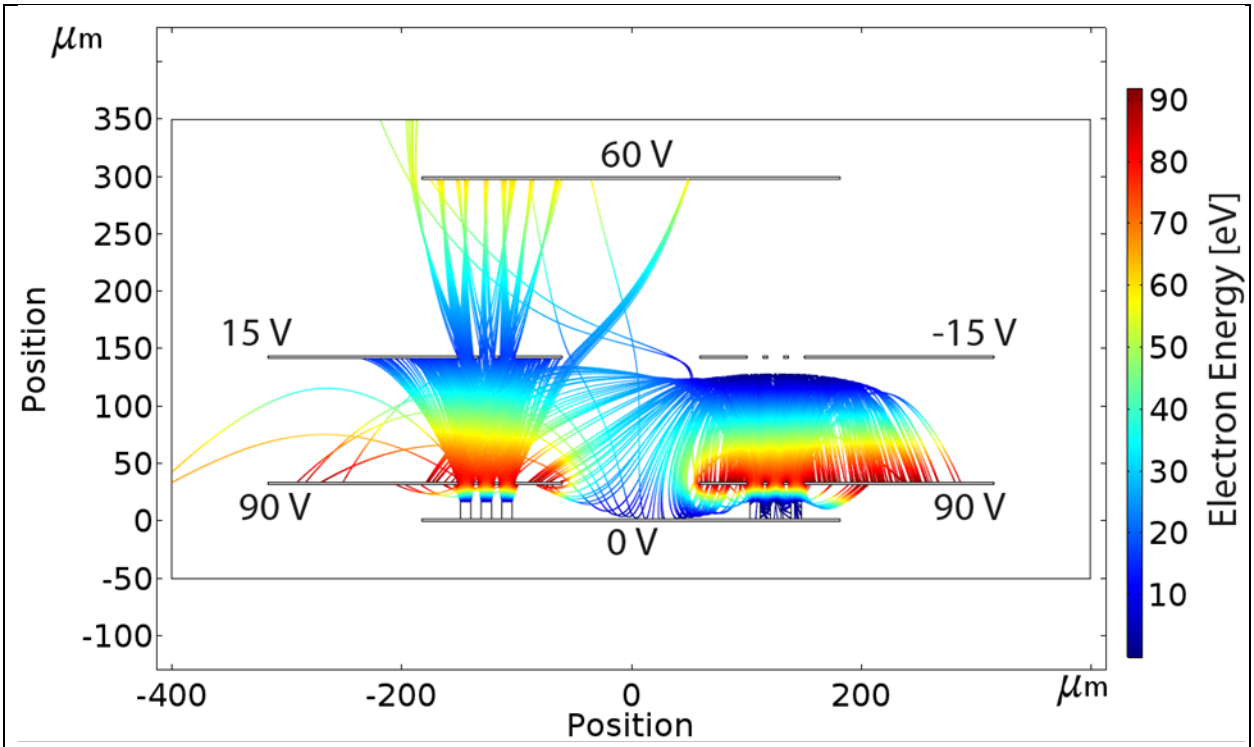

Inputs		Output
A	B	Out
0	0	1
0	1	0
1	0	0
1	1	0

Figure 22. COMSOL simulation of 2-D electron trajectory for the NOR gate with input A on, input B off, where there would be no current through and output load.

5.3.2 CNT emitter characterization

Figure 24 shows the I-V characterization of the field emission from the nanotubes on the cathode each side of the cathode. The measurement uncertainty, shown in green, represents the standard deviation of the cathode current for an average of 10 voltage sweeps. For side A, the turn-on field, the applied field necessary to induce electron emission, was 2.0 V/μm, while for side B the turn-on field was 2.2 V/μm.

Figure 25 (a) and (b) show representative data of the extraction grid potential over time and the corresponding current response for side A while Figure 25 (c) and (d) show extraction grid

potential over time and the corresponding current response for side B. Results show that we can drive a stable current of $1x10^{-7}$ A, with extraction grid A voltage varying between 40 and 93 V for side A, and between 58 and 110 V for side B.

The difference in performance between side A and side B is likely due to differences in morphology of the CNT bundles at the respective sides of the cathode. Even slight differences in CNT morphology can affect their ability to emit current, and CNT films with even slightly different geometries can exhibit different field emission properties [14, 18]. Figure 23 shows an SEM of a representative NOR logic gate. The CNTs on each side of the cathode are labeled and circled in red. From this image it is clear to see the difference in CNT bundle morphology. CNTs on side A of the device have a flatter and more uniform surface at the top of the bundle, while the bundles at side B of the cathode are more irregular.

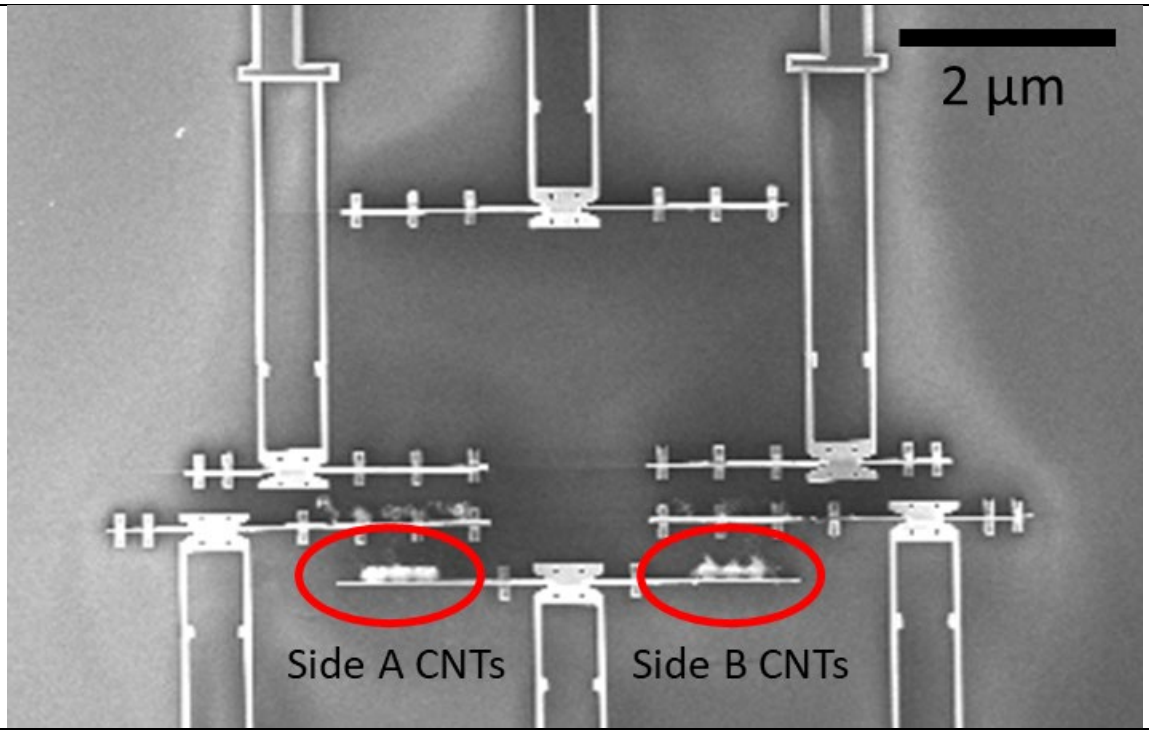

Figure 23: Image of NOR logic gate with CNT bundles labeled and circled in red.

It is unclear what exactly causes this difference in morphology. One potential explanation is differences in the iron catalyst layers on each side of the cathode. 5 nm thick catalyst is evaporated through a shadow mask on each side of the cathode to control where the CNT bundles will be grown [54]. Slight misalignment of the shadow mask, or misalignment of the cathode itself, could lead to a difference in catalyst film thickness. Differences in catalyst film thickness have been shown by Hofmann et. al. to impact CNT bundle morphology [55]. Future work should take care to ensure that iron catalyst deposition is entirely uniform and that CNT bundles are consistent in height and morphology.

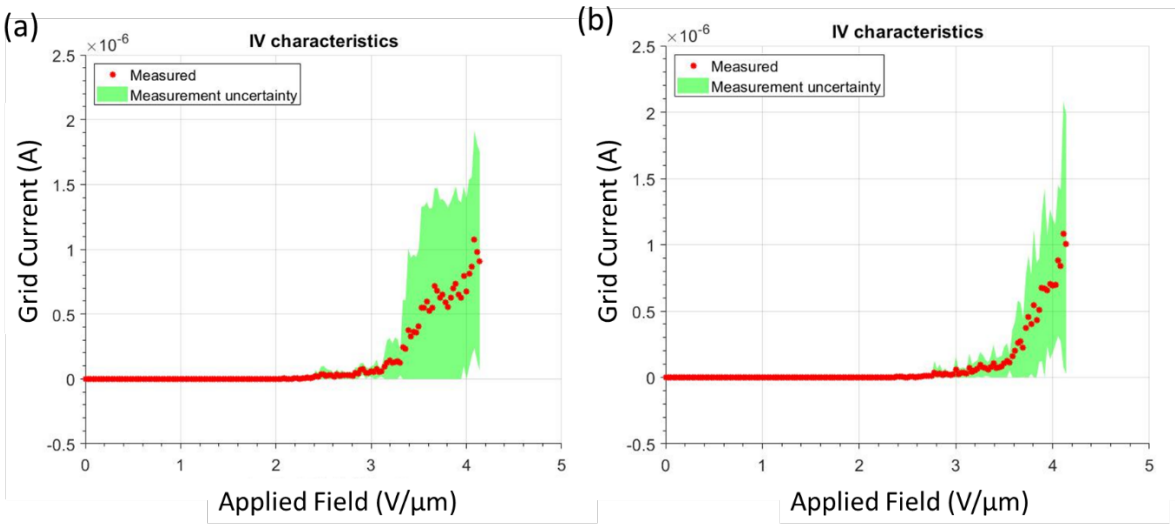

Figure 24: Cathode-to-extraction grid I-V characteristics for Side A (a) and Side B (b) of the NOR gate.

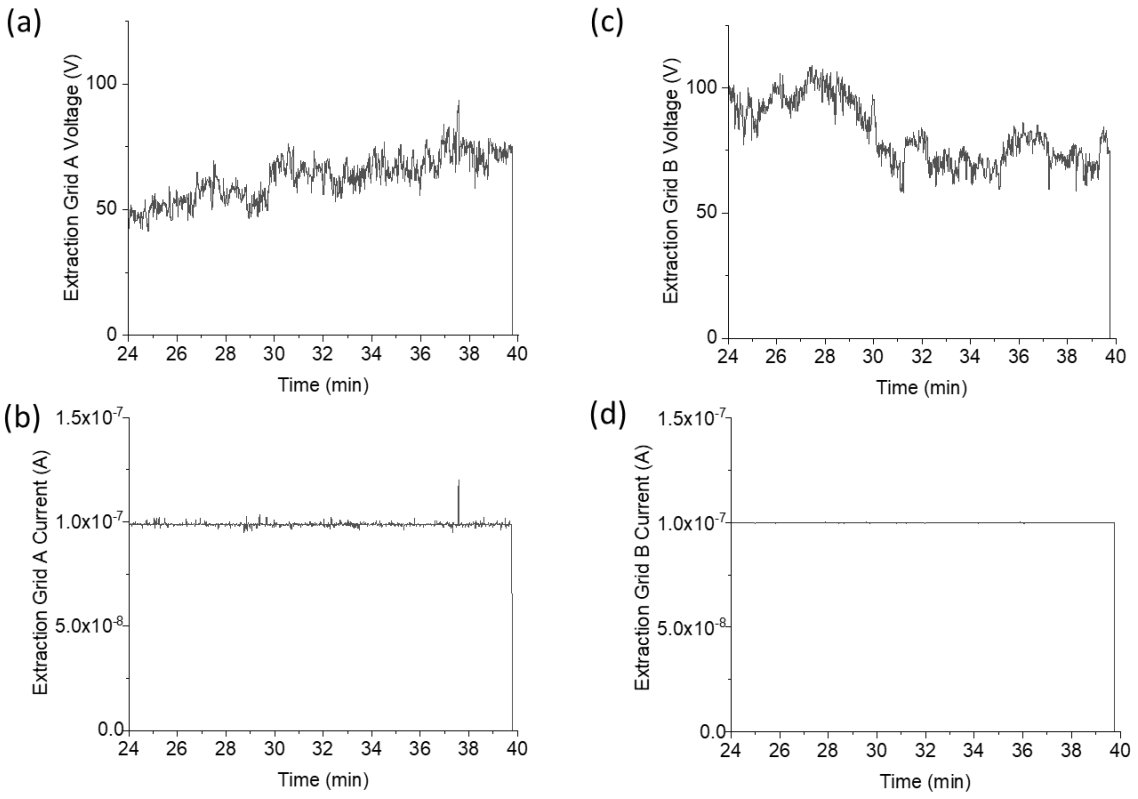

Figure 25: Potential and current response from Extraction Grid A (a and b) and from Extraction Grid B (c and d). Both operating in constant current mode.

5.3.3 Tetrode operation and transistor performance

Figure 26 (a) shows the transistor-like performance of the device when operating as a tetrode. To obtain these curves, the extraction grid extracts a constant current of $1x10^{-6}$ A from the cathode. The Anode voltage is swept from 0-150 V with incrementing stopping grid potentials. The device demonstrates a trend of increasing anode current with increasing stopping grid potential. Transconductance, the measured change in anode current divided by the change in stopping grid voltage, of this device is $7.6x10^{-9}$ S when the cathode is grounded, anode potential is 150 V, and stopping grid voltage is incremented from 10 to 20 V.

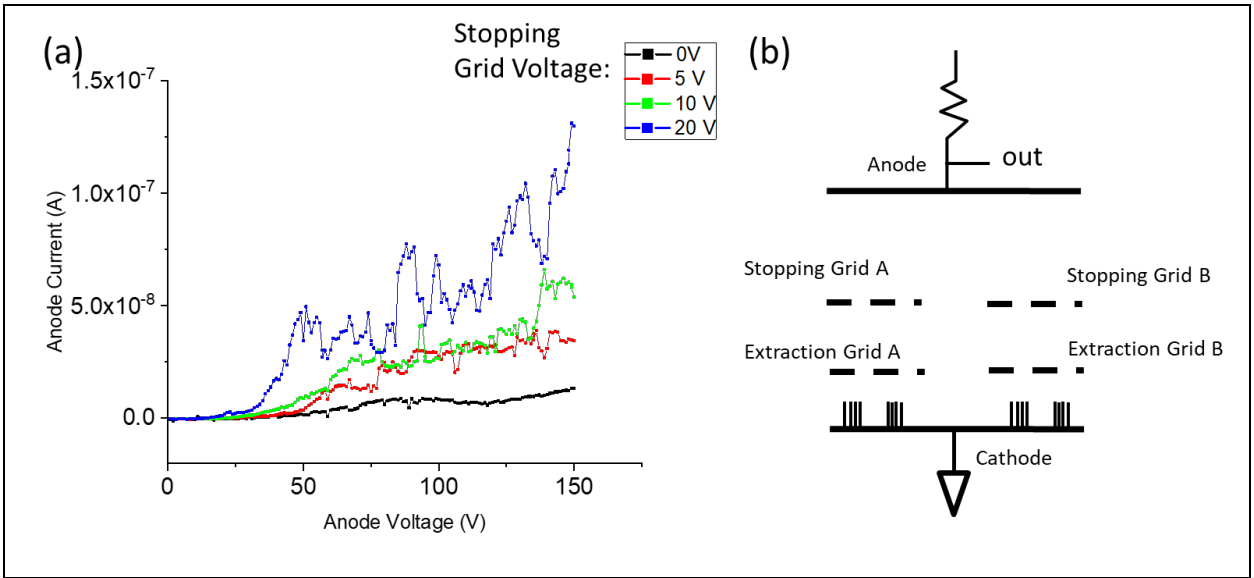

Figure 26: Plot of a representative transistor curve from one side of a NOR gate (a). Schematic of MEMS NOR gate (b).

The relatively low conductance compared to other similar devices reported in literature is due to only a small portion of current leaving the cathode reaching the anode [10, 56]. Figure 27 shows representative data of anode current as a percentage of cathode current. In this case an average of 7.5% of the cathode current makes it through the extraction grid and stopping grid to the anode. This results in more than an order of magnitude decrease in output current that severely affects transconductance of the device. We were also unable to observe anode current saturation in our devices. This is because we are limited in the amount of voltage we can apply to a panel before the panel collapses due to electrostatic forces, which limits our ability to apply biases of >150 V on the anode.

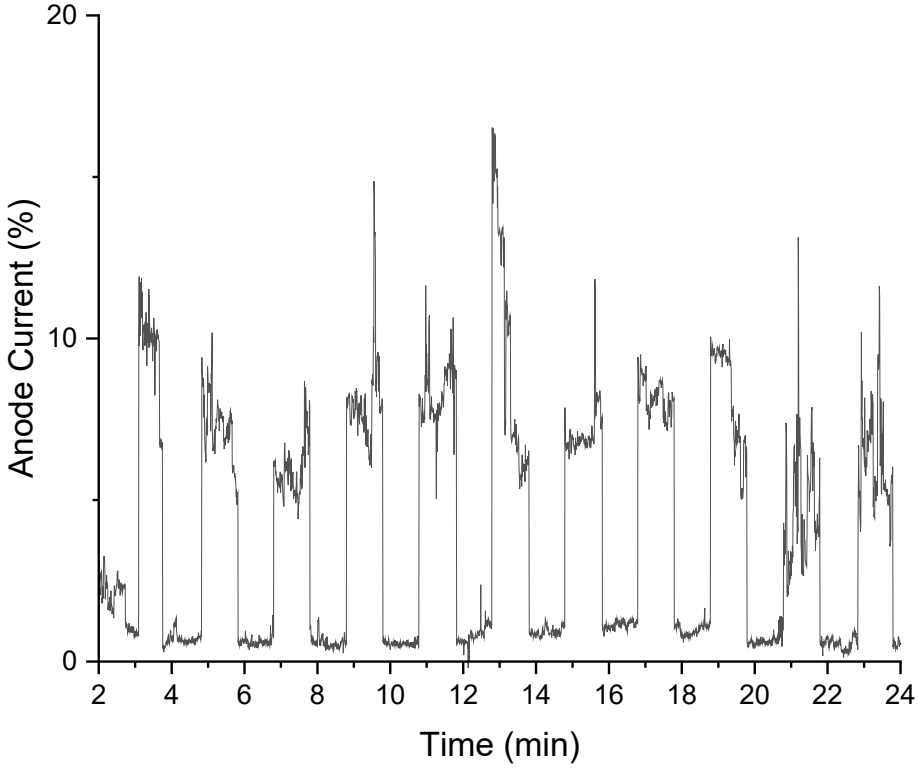

Figure 27: Anode current as a percentage of cathode current during current switching.

Figure 28 shows the tetrode operating in switching mode. In this experiment, the anode voltage is held at 60 V while the stopping grid potentials are modulated from ±5, ±10, and ±15 V over a period of 10 minutes, to turn on and off the anode current. While each bias condition was shown to effectively modulate current at the anode, we determined that for this device, ±10 V was the most effective condition as it was the lowest potential at which we could show clear control of the anode current. With a stopping grid bias below 10V the current noise level makes it difficult to get distinct on/off control of the anode current. Our best performing device, shown in Figure 28, had an on/off anode current ratio of 10.9. This was achieved with anode voltage held at 100 V. This is lower than other field emission-based vacuum microelectronic devices which have demonstrated on/off current ratios in the range of 10^4-10^6 [57, 58].

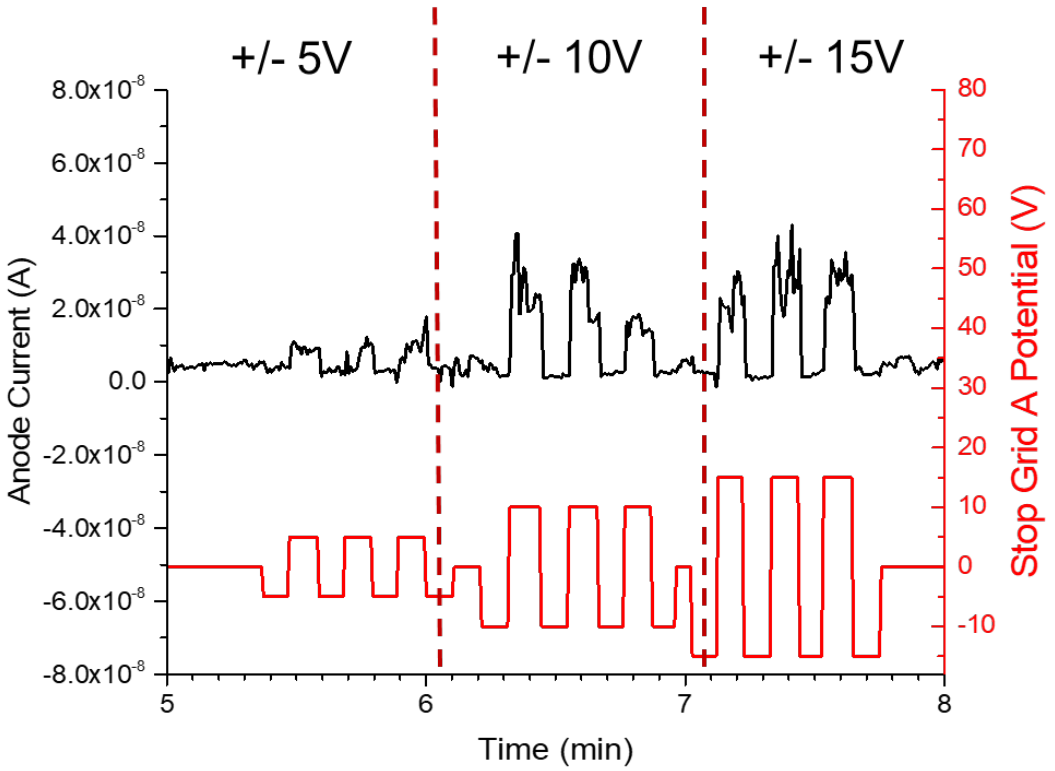

Figure 28: Plot of stopping grid potential and the corresponding current response at the anode.

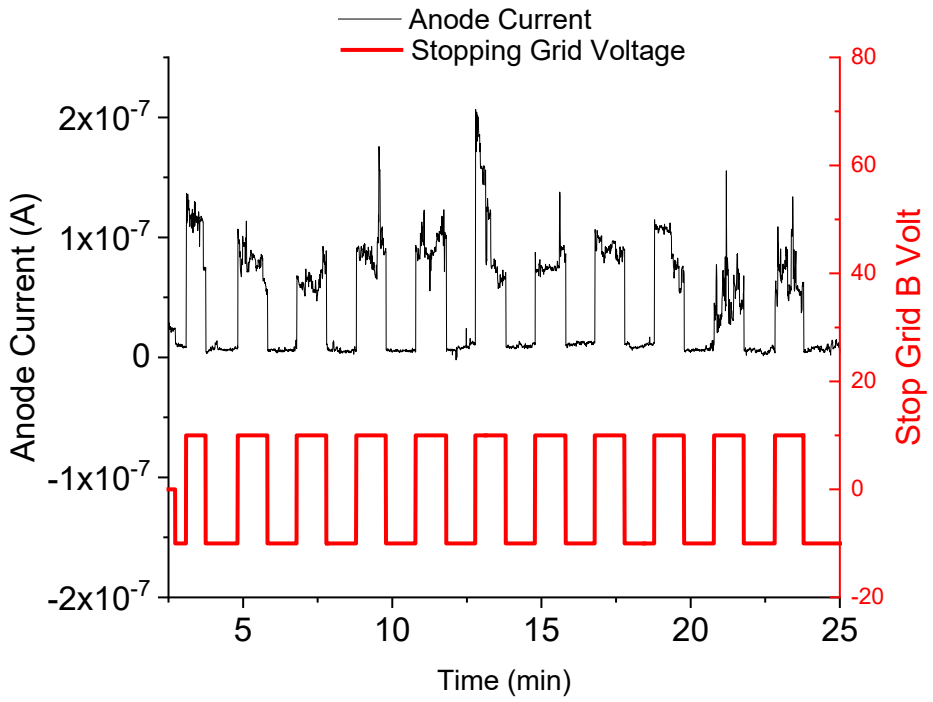

Figure 29: Current switching using stopping grid voltages of +/- 10 V for our best performing device. Average on/off anode current ratio is 10.9.

5.3.4 NOR gate operation

When both sides of the device are operated in parallel, the device operates as a NOR gate. Figure 30 shows NOR gate performance where voltages of ±60 V are applied to stopping grids A and B to modulate current at the anode. Voltages of ±60 V were used to modulate current for this device because, unlike the device shown in Figure 28 and Figure 29, we were unable to modulate this device's current with voltages of ±10 V. It is unclear why different devices perform differently under the same conditions. We will investigate this phenomenon in our future work.

When side A or B are 'on' there is current flowing at the anode, so the anode voltage is low. It is only when both A and B are 'off' that there is no current at the anode. It should be noted that the current from side A and B is not symmetric for reasons described in subsection 5.3.2. Average anode current from side A of the device was approximately 6.8×10^{-9} A, while the average current from side B was 3.5×10^{-8} A. Despite the differences in emission current, this data proves that this device can operate as a NOR gate.

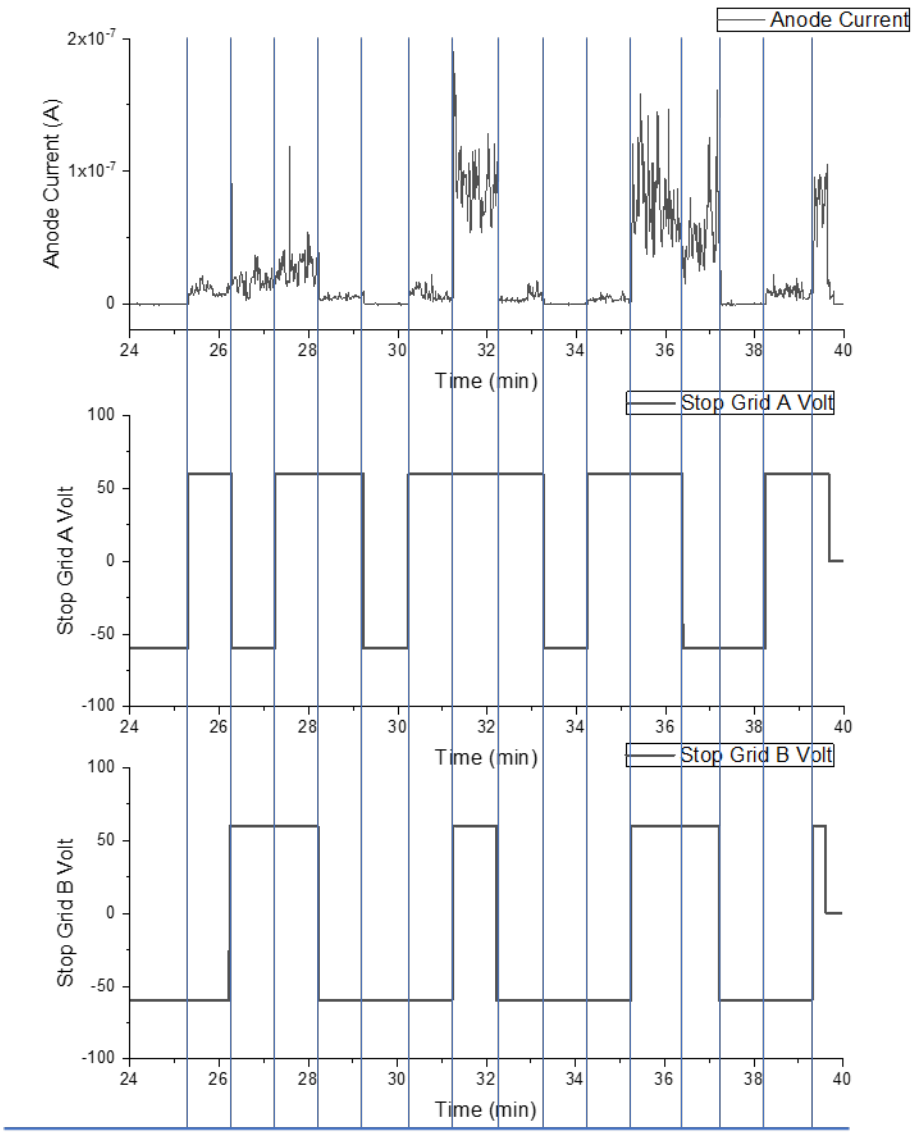

A	0	1	0	1	1	0	1	1	1	0	1	1	0	0	1
B	0	0	1	1	0	0	0	1	0	0	0	1	1	0	0

Figure 30: Demonstrating NOR gate operation with both tetrodes working in parallel.

In summary, we have demonstrated a proof-of-concept NOR logic gate using MEMS processing with aligned CNT field emitters. The device demonstrates an on/off current ratio of up to 10.9 and transconductance of 7.4×10^{-9} S. Our device current response was asymmetric, likely due to variation in CNT field emitter geometry stemming from inconsistent iron catalyst deposition.

Future work will focus on increasing transmission of electrons from the cathode to the anode, as our devices' anode current was less than 10% of the emitted cathode current, with over 90% of current being collected by the extraction and stopping grids. This could be improved by modifying the grid structure to improve electron transmission. Furthermore, improvements can be made to the robustness of the devices, which would allow for larger voltages to be applied to the panels.

6 Future work

6.1 Comparing field emission results of carbon nanostructures

Our work describes field emission performance of aligned CNTs, graphenated CNTs, and aligned-graphenated CNTs, but there are many more carbon nanostructures that can be used as field emitters. Future work should explore other structures, such as graphene nanowall structures, to evaluate their capabilities as field emitters. Some work in literature, such as that by Sankaran et. al., has addressed new carbon nanostructures as field emitters [59], but there is still much work to be done to evaluate different deposition recipes and substrate combinations. Additionally, functionalization of carbon nanostructures, using techniques such as atomic layer deposition, could yield improvements in carbon nanostructure field emission.

6.2 Determination of radiation effects on the MEMS platform

Future work to determine radiation effects on the MEMS platform should expand on the work we have done to include different types of radiation. The effects of proton and electron radiation are still yet to be explored. Additionally, *in situ* experiments to characterize effects of radiation could provide valuable insight as to how radiation affects the MEMS platform during radiation exposure.

6.3 The effects of gamma and proton radiation on aligned CNT field emitters

Our work represents the first experimentation into the effects of proton and gamma radiation on aligned multi-walled CNT field emitter performance. However, there are still many different types of radiation and radiation energy levels that can be explored. In order to fully characterize the effects of gamma and proton radiation on aligned CNT field emitters, future work should focus on experimenting with various proton and gamma radiation sources to fully explore the effects of radiation energy on field emission performance, as well as other radiation sources such as high-energy electrons and ions. Additionally, as discussed in subsection 6.1 other carbon nanostructures may offer benefits over carbon nanotubes as radiation-hardened field emitters.

More work also needs to be done to decouple radiation effects from effects caused by adsorption and desorption of gases on the surface of CNTs. One potential method would to integrate a substrate heater to remove adsorbates from the surface of the CNTs prior to field emission characterization. Combined with an ultra-high vacuum system ($<10^{-9}$ Torr), this would facilitate more consistent CNT field emission performance without interference from adsorbates. This could also be combined with more in-depth characterization of radiation effects on CNT structure using transmission electron spectroscopy.

There is also more work to be done characterizing the effects of radiation on field emitters *in situ.* Our device longevity was severely limited due to constraints of our vacuum system. Future

work should address this with a vacuum system capable of pressure <$1x10^{-6}$ Torr to extend device lifetime and minimize the effects of adsorbates. There is also more work to be done characterizing the effects of radiation on turn-on field and field enhancement factor *in situ*.

6.4 Design, fabrication, and performance characterization of polysilicon MEMS vacuum microelectronic devices

As mentioned in section 5 of this report, our NOR gate devices exhibited poor on/off current ratio and transconductance. Additionally, performance at each side of the device was not symmetrical. These issues are rooted in the fact that less than 10% of the cathode current makes it through the extraction grid and stopping grid to the anode. Future work should focus on improving the anode current. This can be done by optimizing the shape of the extraction and stopping grids to ensure minimal electron current is collected at each of the grid. Furthermore, work to improve CNT bundle uniformity will improve the symmetry of the device performance, as discussed in subsection 5.4. We also observe variation in device performance between different devices with the same structure. The origin of these variations is still unclear, so more experiments are needed to determine why performance varies significantly between devices.

A more capable vacuum system as discussed in subsection 6.3 would also help facilitate *in situ* characterization of radiation effects on vacuum microelectronic device performance. This would allow us to explore the effects of radiation on our MEMS platform and characterize effects such as charge accumulation in the insulating layers that may occur during radiation exposure and affect device performance. Characterizing the detrimental effects of radiation *in situ* would provide better understanding of how these devices will perform in radiative environments and would allow us to make modifications to the device structure that can inhibit any detrimental effects.

7 References

1. Sniegowski, J.J. and M.P. De Boer, *IC-Compatible Polysilicon Surface Micromachining.* Annual Review of Materials Science, 2000. **30**(1): p. 299-333.
2. Jim Carter, A.C., Ramaswamy Mahadevan, Mark Stonefield, Steve Wilcenski, *PolyMUMPs Design Handbook*. 11th Edition, 2005.
3. Amsden, J.J., et al., *Proof of Concept Coded Aperture Miniature Mass Spectrometer Using a Cycloidal Sector Mass Analyzer, a Carbon Nanotube (CNT) Field Emission Electron Ionization Source, and an Array Detector.* Journal of The American Society for Mass Spectrometry, 2018. **29**(2): p. 360-372.
4. Radauscher, E.J., et al., *A miniature electron ionization source fabricated using microelectromechanical systems (MEMS) with integrated carbon nanotube (CNT) field emission cathodes and low-temperature co-fired ceramics (LTCC).* 2016.
5. Stoner, B.R., et al., *A bipolar vacuum microelectronic device.* IEEE Transactions on Electron Devices, 2011. **58**(9): p. 3189-3194.
6. Radauscher, E.J., et al., *Improved Performance of Field Emission Vacuum Microelectronic Devices for Integrated Circuits.* IEEE Transactions on Electron Devices, 2016. **63**(9): p. 3753-3760.

7. Shea, H.R., *Radiation sensitivity of microelectromechanical system devices.* Journal of Micro/Nanolithography, MEMS, and MOEMS, 2009. **8**(3): p. 031303.
8. Caffey, J.R. and P.E. Kladitis. *The effects of ionizing radiation on microelectromechanical systems (MEMS) actuators: electrostatic, electrothermal, and bimorph*. in *17th IEEE International Conference on Micro Electro Mechanical Systems*. 2004. Maastricht, Netherlands, Netherlands IEEE.
9. Schwank, J.R., et al., *Radiation Effects in MOS Oxides.* IEEE Transactions on Nuclear Science, 2008. **55**(4): p. 1833-1853.
10. Natarajan, S., et al., *High voltage microelectromechanical systems platform for fully integrated, on-chip, vacuum electronic devices.* Applied Physics Letters, 2008. **92**(22): p. 1-4.
11. Calderón-Colón, X., et al., *A carbon nanotube field emission cathode with high current density and long-term stability.* Nanotechnology, 2009. **20**(32).
12. de Heer, W.A., A. Châtelain, and D. Ugarte, *A Carbon Nanotube Field-Emission Electron Source.* Science, 1995. **270**(5239): p. 1179-1180.
13. Ubnoske, S.M., et al., *Perspectives on the growth of high edge density carbon nanostructures: Transitions from vertically oriented graphene nanosheets to graphenated carbon nanotubes.* Journal of Physical Chemistry C, 2014. **118**(29): p. 16126-16132.
14. Bonard, J.-M., et al., *Field emission properties of multiwalled carbon nanotubes.* Ultramicroscopy, 1998. **73**: p. 7-15.
15. Cui, H., O. Zhou, and B.R. Stoner, *Deposition of aligned bamboo-like carbon nanotubes via microwave plasma enhanced chemical vapor deposition.* Journal of Applied Physics, 2000. **88**(10): p. 6072-6074.
16. De Jonge, N., et al., *Low noise and stable emission from carbon nanotube electron sources.* Applied Physics Letters, 2005. **87**(13): p. 133118.
17. Yeong, K.S. and J.T.L. Thong, *Effects of adsorbates on the field emission current from carbon nanotubes.* Applied Surface Science, 2004. **233**(1-4): p. 20-23.
18. Cheng, Y. and O. Zhou, *Electron field emission from carbon nanotubes.* 2003. **4**: p. 1021-1033.
19. Teo, K.B.K., et al., *Field emission from dense , sparse , and patterned arrays of carbon nanofibers.* 2011. **80**(11): p. 2011-2013.
20. Chockalingam, S., et al., *Synthesis, structural and field emission properties of multiwall carbon nanotube-graphene-like nanocarbon hybrid films grown by microwave plasma enhanced chemical vapor deposition.* Materials Chemistry and Physics, 2015. **156**: p. 38-46.
21. Bonard, J.-m., et al., *Field emission properties of multiwalled carbon nanotubes.* 1998. **73**: p. 7-15.
22. Zhu, W., et al., *Large current density from carbon nanotube field emitters.* Applied Physics Letters, 1999. **75**(6): p. 873-875.
23. Chen, L., et al., *Electron field emission characteristics of graphene/carbon nanotubes hybrid field emitter.* Journal of Alloys and Compounds, 2014. **610**: p. 659-664.
24. Fowler, R.H. and L. Nordheim, *Electron Emission in Intense Electric Fields.* Proceedings of the Royal Society. A, Mathematical, physical, and engineering sciences, 1928. **119**(781): p. 173-181.
25. Spindt, C.A., et al., *Physical properties of thin-film field emission cathodes with molybdenum cones.* Journal of Applied Physics, 1976. **47**(12): p. 5248-5263.

26. Utsumi, T., *Vacuum microelectronics: What's new and exciting.* IEEE Transactions on Electron Devices, 1991. **38**(10): p. 2276-2283.
27. Chouhan, V., T. Noguchi, and S. Kato, *Field emission from optimized structure of carbon nanotube field emitter array.* Journal of Applied Physics, 2016. **119**(13): p. 134303-134303.
28. Chen, P.H., et al., *Characterization and enhanced field emission properties of carbon nanotube bundle arrays coated with N-doped nanocrystalline anatase TiO2.* Materials Chemistry and Physics, 2014. **143**(3): p. 1378-1383.
29. Gupta, S., et al., *Electron field emission properties of gamma irradiated microcrystalline diamond and nanocrystalline carbon thin films.* Journal of Applied Physics, 2002. **92**(6): p. 3311-3317.
30. Khare, B., et al., *Proton Irradiation of Carbon Nanotubes.* Nano Letters, 2003. **3**(System 2000): p. 643-646.
31. Li, B., et al., *The effect of gamma ray irradiation on the structure of graphite and multi-walled carbon nanotubes.* Carbon, 2013. **60**(0): p. 186-192.
32. Dresselhaus, M.S., et al., *Raman spectroscopy of carbon nanotubes.* Physics Reports, 2005. **409**(2): p. 47-99.
33. Dresselhaus, M.S., et al., *Perspectives on carbon nanotubes and graphene Raman spectroscopy.* Nano Letters, 2010. **10**(3): p. 751-758.
34. Jorio, A., et al., *Characterizing carbon nanotube samples with resonance Raman scattering.* New Journal of Physics, 2003. **5**(1): p. 139.1-139.17.
35. Lu, X., et al., *Nonlinear fowler-nordheim plots of the field electron emission from graphitic nanocones: Influence of non-uniform field enhancement factors.* Journal of Physics D: Applied Physics, 2006. **39**(15): p. 3375-3379.
36. Sun, Y., D.A. Jaffray, and J.T.W. Yeow, *Self-heating Schottky emission from a ballasted carbon nanotube array.* Carbon, 2013. **58**: p. 87-91.
37. Matthews, M.J. and M.A. Pimenta, *Origin of dispersive effects of the Raman D band in carbon materials.* 1999. **59**(10): p. 6585-6588.
38. Safibonab, B., et al., *Improving the surface properties of multi-walled carbon nanotubes after irradiation with gamma rays.* Applied Surface Science, 2011. **258**(2): p. 766-773.
39. Lee, S.-F., Y.-P. Chang, and L.-Y. Lee, *Plasma treatment effects on surface morphology and field emission characteristics of carbon nanotubes.* Journal of Materials Science: Materials in Electronics, 2008. **20**(9): p. 851-857.
40. Patil, S.S., et al., *Influence of high-energy electron irradiation on field emission properties of multi-walled carbon nanotubes (MWCNTs) films.* Physica B: Condensed Matter, 2011. **406**(9): p. 1809-1813.
41. Kim, W.S., et al., *Relationship between field-emission characteristics and defects measured by Raman scattering in carbon-nanotube cathodes treated by plasma and laser.* Journal of Vacuum Science & Technology B: Microelectronics and Nanometer Structures Processing, Measurement, and Phenomena, 2008. **26**(2): p. 760-763.
42. Becker, J.A. and J.N. Shive, *The transistor — A new semiconductor amplifier.* Electrical Engineering, 1949. **68**(3): p. 215-221.
43. Dimitrijev, S., *Analysis of gamma-radiation induced instability mechanisms in cmos transistors.* Solid-State Electronics, 1989. **32**(5): p. 349-353.

44. Serbun, P., et al., *Stable field emission of single B-doped Si tips and linear current scaling of uniform tip arrays for integrated vacuum microelectronic devices.* Journal of Vacuum Science & Technology B, 2013. **31**(2): p. 02B101.
45. Rozhnev, A.G., et al., *Novel concepts of vacuum microelectronic microwave devices with field emitter cathode arrays.* Physics of Plasmas, 2002. **9**(9): p. 4020-4027.
46. Nicolaescu, D. and V. Filip, *Vacuum microelectronics devices based on the controlled electron motion in electric and magnetic fields.* The European Physical Journal Applied Physics, 2000. **10**(1): p. 33-42.
47. Shen, Z., et al., *A new kind of vertically aligned field emission transistor with a cylindrical vacuum channel.* Vacuum, 2017. **137**: p. 163-168.
48. Jones, W.M., D. Lukin, and A. Scherer, *Practical nanoscale field emission devices for integrated circuits.* Applied Physics Letters, 2017. **110**(26).
49. Ding, M.Q., et al., *Fabrications of Spindt-type cathodes with aligned carbon nanotube emitters.* Applied Surface Science, 2005. **251**(1-4): p. 201-204.
50. Guglielmotti, V., et al., *Macroscopic self-standing SWCNT fibres as efficient electron emitters with very high emission current for robust cold cathodes.* Carbon, 2013. **52**: p. 356-362.
51. Subramanian, K., et al., *Field emission devices for advanced electronics comprised of lateral nanodiamond or carbon nanotube emitters.* Diamond and Related Materials, 2007. **16**(12): p. 1997-2002.
52. Bower, C., et al., *On-chip vacuum microtriode using carbon nanotube field emitters.* Applied Physics Letters, 2002. **80**(20): p. 3820-3822.
53. Gilchrist, K.H., et al., *Platform for integrated vacuum microelectronic circuits.* IEEE International Vacuum Electronics Conference, IVEC 2014, 2014: p. 155-156.
54. Bower, C.A., et al., *On-chip electron-impact ion source using carbon nanotube field emitters.* Applied Physics Letters, 2007. **90**(12): p. 1-4.
55. Hofmann, S., et al., *Effects of catalyst film thickness on plasma-enhanced carbon nanotube growth.* Journal of Applied Physics, 2005. **98**(3).
56. Caffey, J.R., *The Effects of Ionizing Radiation on Microelectromechanical Systems (MEMS) Actuators: Electrostatic, Electrothermal, and Residual Stress*, in *Department of the Air Force*. 2003, Air Force Institute of Technology: Defense Technical Information Center. p. 217.
57. Han, J.-W., J.S. Oh, and M. Meyyappan, *Cofabrication of Vacuum Field Emission Transistor (VFET) and MOSFET.* IEEE Transactions on Nanotechnology, 2014. **13**(3): p. 464-468.
58. Tsai, J.T.H. and J.G.S. Li, *Fabrication and Characterization of Carbon Nanotubes Integrated on Field-Emission Diode.* IEEE Electron Device Letters, 2008. **29**(7): p. 691-693.
59. Sankaran, K.J., et al., *Self-organized multi-layered graphene–boron-doped diamond hybrid nanowalls for high-performance electron emission devices.* Nanoscale, 2018: p. 1345-1355.